Direct Measurements of Concentration and Velocity in the Richtmyer-Meshkov Instability

By

Daniel T. Reese

A DISSERTATION SUBMITTED IN PARTIAL FULFILLMENT OF THE

REQUIREMENTS FOR THE DEGREE OF

DOCTOR OF PHILOSOPHY

(ENGINEERING MECHANICS)

at the

UNIVERSITY OF WISCONSIN – MADISON

2017

Date of final oral examination: 06/21/17

The dissertation is approved by the following members of the Final Oral Committee:
    Riccardo Bonazza, Professor, Engineering Physics
    Leslie Smith, Professor, Mathematics
    David Rothamer, Assistant Professor, Mechanical Engineering
    Gregory Moses, Professor, Engineering Physics
    Christopher Rutland, Professor, Mechanical Engineering

ProQuest Number: 10601826

ProQuest®

ProQuest 10601826

Abstract

The development of the Richtmyer-Meshkov instability (RMI) is experimentally investigated in a vertical shock tube using a broadband initial condition imposed on an interface between a helium-acetone mixture and argon (Atwood number $A \approx 0.7$). The shear layer used in the present work serves as a statistically repeatable, broadband initial condition to the RMI, and is accelerated by either an $M = 1.6$ or $M = 2.2$ planar shock wave. The development of the ensuing mixing layer is investigated using simultaneous planar laser-induced fluorescence (PLIF) and particle image velocimetry (PIV). PLIF images are processed to reveal the light-gas mole fraction, while PIV particle image pairs yield corresponding full-field velocity results. Field structure and distribution is explored through probability density functions (PDFs), and a decomposition is performed on concentration and velocity results to obtain a mean flow field and define fluctuations. Simultaneous concentration and velocity field measurements allow – for the first time in this regime – experimentally determined turbulence quantities such as Reynolds stresses, turbulent mass-flux velocities, and turbulent kinetic energy. We show that by the latest times the mixing layer has passed the turbulent threshold, and there is evidence of turbulent mixing occuring sooner for the higher Mach number case. Interface measurements show nonlinear growth with a power-law fit to the thickness data, and integral measurements of mixing layer thickness are proportional to threshold measurements. Spectral analysis demonstrates the emergence of an inertial range with a slope $\sim k^{-5/3}$ when considering both density and velocity effects in planar turbulent kinetic energy (TKE) measurements.

Acknowledgements

I would like to extend my sincerest thanks to my advisor, Professor Riccardo Bonazza, for the never-ending patience, support, encouragement, guidance, and wisdom he has offered throughout my time in graduate school. Having Professor Bonazza as a mentor and friend has made my time as a Ph.D. student truly enjoyable, and I cannot overstate the importance of our relationship to my success over the past five years.

I am incredibly grateful to have had the additional support and advice of Dr. Jason Oakley and Professor David Rothamer during my time at the College of Engineering. Dr. Oakley was always willing to make time for our impromptu discussions, and his extensive knowledge of the shock tube has saved the day more times than I can count. Professor Rothamer never failed to provide his experimental know-how and invaluable expertise on camera systems and lasers when needed the most.

Thank you to my fellow graduate students Josh Herzog, Alex Ames, and Chris Noble who shared in my ecstasy when things went right, and wallowed in misery with me when things inevitably did not. I am also thankful for the help provided by the undergraduate students Gunnar Thompson, Mitch Corcoran, and Sam Szotkowski, who generously gave up their free time to spend long nights and weekends with me in the lab.

Most importantly, thank you to my entire family and amazing girlfriend Brooke; your enduring love and support throughout this process were, at times, all that kept me motivated to continue working toward my goals. Without you, I never would have made it.

Contents

List of Figures

List of Tables

Nomenclature

Abbreviations

ACCIV   Advection Corrected Correlation Image Velocimetry

CIV   Correlation Image Velocimetry

DT   Deuterium-tritium

FAV   Fast-acting valve

FFT   Fast Fourier transform

IC   Initial condition time/location

ICF   Inertial confinement fusion

LANL   Los Alamos National Laboratory

LES   Large-eddy simulation

LLNL   Lawrence Livermore National Laboratory

PDF   Probability density function

PIV   Particle image velocimetry

PLIF   Planar laser-induced fluorescence

PLV   Pulsed-light velocimetry

PS1   First post-shock time/location

PS2   Second post-shock time/location

PS3   Third post-shock time/location

PS4   Fourth post-shock time/location

RMI   Richtmyer-Meshkov instability

RMS   Root mean square

RTI   Rayleigh-Taylor instability

WiSTL   Wisconsin shock tube laboratory

English Symbols

a Single mode perturbation amplitude

a_0 Single mode perturbation amplitude at $t = 0$

A Atwood number across the interface

$\mathscr{D}$ Diffusion coefficient

$E(k)$ One-dimensional scalar variance energy spectrum

E_f Energy spectrum of the variable f

$F()$ Fourier coefficient

$F^*()$ Complex conjugate of the Fourier coefficient

k	Wavenumber
K	Velocity-derivative kurtosis
M	Mach number of incident shock wave
p	Pressure
Re	Reynolds number
Re_λ	Taylor Reynolds number
S	Velocity-derivative skewness
S_f	Fluorescence signal
t	Time after shock traverses the interface
T	Temperature
$\boldsymbol{u}$	Velocity vector
$\boldsymbol{u}'$	Velocity-flucuation vector
u	x-component of velocity
u'	x-component of velocity-flucuation
v	y-component of velocity
v'	y-component of velocity-flucuation
V_0	Post-shock 1D interface velocity

w	z-component of velocity
w'	z-component of velocity-flucuation
$\boldsymbol{x}$	Position vector
x	x-component of position
y	y-component of position
z	z-component of position

Greek Symbols

δ	Diffusion length
η_k	Kolmogorov length scale
λ	Wavelength
λ_B	Batchelor scale
λ_T	Taylor microscale
μ	Mean
ν	Kinematic viscosity
ξ	Mole fraction
Ξ	Mixedness ratio
ρ	Density

ρ_1 Light gas density

ρ_2 Heavy gas density

σ Standard deviation

$\underline{\tau}$ Viscous stress tensor

τ_D Characteristic diffusion time

$\boldsymbol{\omega}$ Vorticity vector

Chapter 1

Introduction

It has been said that "turbulence is probably the most important and yet least understood problem in classical physics" [56]; a deeper understanding of this phenomenon, along with a better comprehension of its development, is vital to the forward progress of turbulence's many and far-reaching fields of applicability. The present work will focus on the development of concentration and velocity in a turbulent mixing layer caused by the impulsive acceleration of an interface between two fluids of different density. The production, evolution, and ultimate decay of this turbulent zone is governed by the Richtmyer-Meshkov instability (RMI), which plays out over a large span of both length and time scales, and appears in a large variety of applications.

First theorized by Richtmyer in 1960 [69], and later validated by the experiments of Meshkov [48, 49], the RMI has puzzled scientists for years, prompting many decades of research into the subject. Early experimental work used wire mesh and membranes to seperate the test gases prior to shock acceleration, and information about the mixing region was limited to integrated line-of-sight measurements of the mixing zone. As researchers realized that the mesh and membrane greatly impacted the flow, methods of creating membraneless interfaces were developed, and integrated measurements eventually gave way to planar laser measurements.

The work detailed in this report seeks to add to the ongoing progress of this ever-evolving

field by making direct, simultaneous planar measurements of several variables important in shock accelerated inhomogeneous flows. The RMI is experimentally investigated at several stages in its development in the Wisconsin Shock Tube Laboratory (WiSTL) to provide insight into the concentration and velocity fields that result from impulsively accelerating the broadband interface between a light and heavy gas. This report begins with background into the physics of the RMI, motivation for its study, and previous work in Chapter 2. Chapter 3 describes the current experiment, including information about the WiSTL facility, the initial condition, and the experimental configuration used to obtain information about the flow. Chapter 4 discusses the processing steps used to obtain concentration measurements from PLIF data, velocity data from PIV particle image pairs, matching of the two fields, and a decomposition of the flow into mean and fluctuating components. Results and a discussion of their significance are presented in Chater 5, and a summary of important findings and conclusions are given in Chapter 6.

Chapter 2

Background

2.1 The Richtmyer-Meshkov Instability

The Richtmyer-Meshkov instability (RMI) [69, 48] occurs when a shock wave passes through the interface between two fluids of different density. Vorticity is deposited during shock acceleration of the interface through the misalignment of pressure and density gradients, and this vorticity drives the growth of perturbations, ultimately leading to enhanced mixing of the fluids at late times. This instability involves several fundamental compressible fluid dynamic concepts, including shock dynamics, vorticity deposition, interface deformation, and, at late times, the growth of secondary instabilities that lead to turbulent mixing. In this chapter, the origin of the instability is viewed through the vorticity transport equation in section 2.1.1, the growth of perturbations is considered in section 2.1.2, and the resultant turbulent mixing is explored in section 2.1.3. Motivation for studying the RMI is given in section 2.2, and an overview of important previous research is provided in section 2.3.

2.1.1 Vorticity Deposition

The genesis, development, and decay of the Richtmyer-Meshkov instability is governed by the vorticity transport equation,

$$\frac{D\boldsymbol{\omega}}{Dt} = (\boldsymbol{\omega} \cdot \nabla)\,\boldsymbol{u} - \boldsymbol{\omega}\,(\nabla \cdot \boldsymbol{u}) + \nu\nabla^2\boldsymbol{\omega} + \frac{1}{\rho^2}\,(\nabla\rho \times \nabla p)\,, \tag{2.1}$$

where ρ is the density, p is the pressure, ν is the viscosity, $\boldsymbol{u} \equiv (u, v, w)$ is the velocity vector and $\boldsymbol{\omega} \equiv \boldsymbol{\nabla} \times \boldsymbol{u}$ is the vorticity. The last term on the right-hand side is called the baroclinic production term, and leads to a production of vorticity when $|\boldsymbol{\nabla}p \times \boldsymbol{\nabla}\rho| > 0$. The first term on the right hand side is the vortex stretching term; it represents the enhancement of vorticity by stretching and is only present in three-dimensional flows. Vortex stretching is the mechanism by which turbulent energy is transferred to smaller scales. The second term on the right hand side of Eq. (2.1) is the expansion term. In an expanding flow, $\nabla \cdot \boldsymbol{u} > 0$, resulting in a decrease in the magnitude of vorticity, while if the fluid is under compression, $\nabla \cdot \boldsymbol{u} < 0$, and vorticity will increase. Finally, the third term on the right hand side of the equation is the diffusion term; this term describes the effects of viscous diffusion on the vorticity distribution.

Since the interaction of the shock wave with the interface occurs at much shorter time scales than the evolution of the instability, the baroclinic production term can be separated from the rest of Eq. (2.1) [80] to find,

$$\frac{\partial\boldsymbol{\omega}}{\partial t} \approx \frac{1}{\rho^2}\boldsymbol{\nabla}\rho \times \boldsymbol{\nabla}p, \tag{2.2}$$

where the pressure gradient can be determined through the momentum equation

$$\frac{\partial\rho\boldsymbol{u}}{\partial t} + \boldsymbol{\nabla} \cdot (\rho\boldsymbol{u}\boldsymbol{u}) = -\boldsymbol{\nabla} \cdot (p\underline{\boldsymbol{\delta}}) + \boldsymbol{\nabla} \cdot \underline{\boldsymbol{\tau}}, \tag{2.3}$$

where $\underline{\boldsymbol{\tau}}$ is the viscous stress tensor and $\underline{\boldsymbol{\delta}}$ is the unit tensor. See Fig. 1 for axis orientation. By neglecting the viscous and nonlinear terms in Eq. (2.3) and assuming that the shock remains planar, the pressure gradient becomes:

$$\frac{\partial p}{\partial x} \approx 0\,, \tag{2.4}$$

$$\frac{\partial p}{\partial y} \approx 0 \, , \tag{2.5}$$

$$\frac{\partial p}{\partial z} \approx -\frac{\partial \rho w}{\partial t} \, , \tag{2.6}$$

where the shock normal and the interface normal directions are aligned with the z-axis. By inserting these values into Eq. (2.2) and taking the post-shock interface velocity to be V_0, then one can integrate over the impulse to get

$$\omega_x \approx \frac{V_0}{\rho} \frac{\partial \rho}{\partial y}, \tag{2.7}$$

$$\omega_y \approx -\frac{V_0}{\rho} \frac{\partial \rho}{\partial x}, \tag{2.8}$$

$$\omega_z \approx 0. \tag{2.9}$$

If the interface is 2D, then $\omega_x = 0$ and the vorticity deposition can be approximated using only the the density field and the 1D post-shock interface velocity.

While previous studies have relied heavily on the above analysis in order to obtain vorticity deposition measurements from concentration fields [81, 85], the work outlined in this report will not require the numerous assumptions made in order to obtain vorticity measurements in this way. Instead, direct measurements of vorticity are made by capturing the velocity field concurrently with concentration measurements. The particle image velocimetry (PIV) method used in the current work only captures velocities perpendicular to the line-of-sight of the camera, and so the velocity component in the third direction remains unknown. Using the two measured components of velocity, the out-of-plane vorticity can be obtained simply by taking the curl of the velocity field, $\boldsymbol{\omega} \equiv \boldsymbol{\nabla} \times \boldsymbol{u}$.
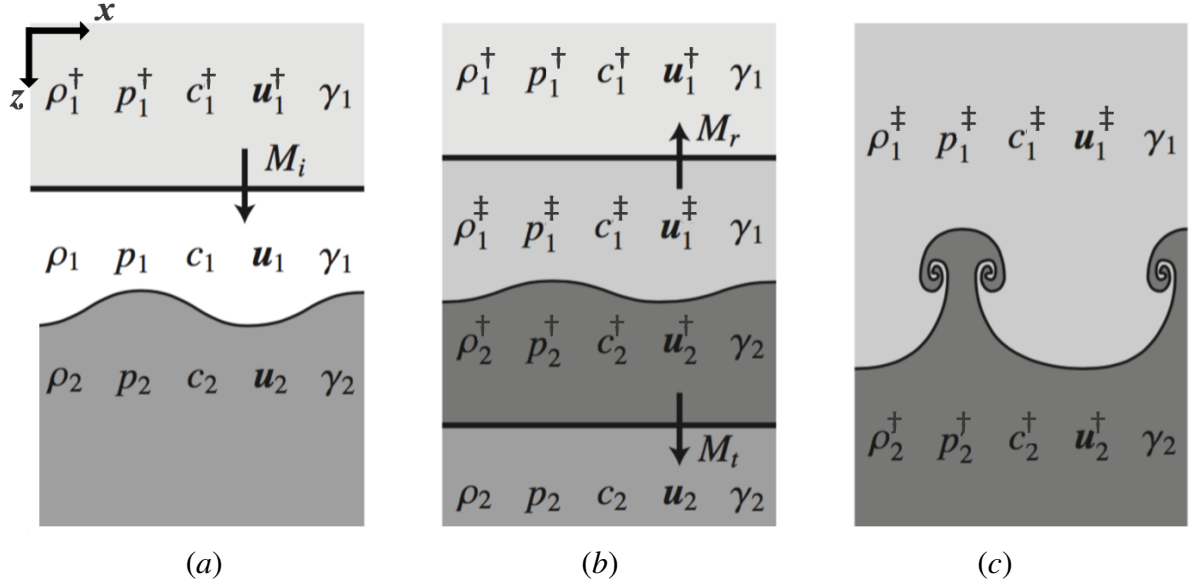
Figure 1: Schematic showing the development of the RMI. Daggers (†) indicate a gas has been shocked, while double daggers (‡) represent twice-shocked gas (by shock and reshock) and darker shading indicates higher density.

2.1.2 Perturbation Growth

Vorticity deposition following the impulsive acceleration will cause the growth of any perturbations present at the interface. A visual representation of the RMI is shown in Fig. 1, which depicts the perturbation and incoming shock wave in (a), the reflected and transmitted shock wave in (b), and the development of spike and bubble structures due to the growth and roll-up of the perturbations caused by the instability in (c). The parameters of interest include the density, ρ, pressure, p, speed of sound, c, ratio of specific heats, γ, and the velocity $\boldsymbol{u} = u\hat{x} + v\hat{y} + w\hat{z}$. Daggers denote the number of times a region of fluid has been traversed by a shock wave, while different subscripts indicate a given fluid.

The simplified visualization of the RMI shown in Fig. 1 considers only two-dimensional perturbations of a single wavelength and amplitude, while the experiments conducted in the

present work involve a broadband interface, consisting of many three-dimensional perturbations containing a variety of different wavelengths and amplitudes. This will cause the development of a turbulent mixing zone at late times, rather than clearly defined spike and bubble structures; nevertheless, the governing physics of the instability remain similar for both the multimode and single perturbation cases.

Following passage of the shock wave, the growth of perturbations on the interface is initially linear in time. As the instability develops and the amplitudes of perturbations become large, eventually their growth becomes nonlinear, and a turbulent mixing zone will develop between the two fluids at late times. Taking the peak-to-trough height of a perturbation to be η, and a peak-to-peak wavelength defined by λ, the wavenumber (k) of a perturbation is given by,

$$k = \frac{2\pi}{\lambda}. \tag{2.10}$$

Beginning with Taylor's incompressible, linear theory for the growth of small perturbations ($\eta << \lambda$) under gravitational acceleration, g,

$$\frac{d^2\eta(t)}{dt^2} = kgA\eta(t), \tag{2.11}$$

where $A = \frac{\rho_1 - \rho_2}{\rho_1 + \rho_2}$ is the Atwood number, Richtmyer first replaced the constant g by an impulsive acceleration. Taking $g = V_0\delta(t)$, where V_0 is the post-shock 1D interface velocity, and integrating Eq. (2.11) with respect to time, Richtmyer found the impulsive growth rate to be given by,

$$\dot{\eta} = kV_0A\eta_0 \tag{2.12}$$

where η_0 is the perturbation amplitude at $t=0$. We note that this is unstable for all A; for $A > 0$ there is immediate growth of the perturbation, while for $A < 0$ there is first a phase reversal, followed by growth.

In addition to the linear growth at early times following impulsive acceleration of small perturbations, an understanding of growth in the nonlinear regime has been long sought-after. Though many investigators agree to a power law growth of the mixing zone height, h, as $h \sim t^\theta$, a number of values for θ have been reported [25, 26, 60, 85, 38]. This power law relationship describing mixing layer growth can be derived beginning with the kinetic energy per unit area of the layer,

$$K = \frac{1}{2}\rho h V^2, \tag{2.13}$$

where h is the length scale, V is the velocity magnitude, and ρ is the density. The dissipation of kinetic energy is given by

$$\frac{dK}{dt} = -cKV/h, \tag{2.14}$$

which can also be written,

$$\frac{d}{dt}\left(hV^2\right) = -cV^3, \tag{2.15}$$

where c is a coefficient describing dissipation. Since the width of the mixing layer can be related to the velocity through $\dfrac{dh}{dt} = V$, the solution to the above equations is $h \propto t^\theta$, where $\theta = \dfrac{2}{3+c}$.

Despite decades of research into the Richtmyer-Meshkov instability there are still many unanswered questions that remain. Does the turbulent mixing zone growth in the nonlinear regime truly follow a relation as $h \sim t^\theta$, and if so, what is the value of θ? With such a large variation in reported values of the growth factor [25, 26, 60, 85, 38], how sensitive is this value to initial conditions and flow parameters? Current experimental evidence has thus far been unable to answer these questions, among others, and it is therefore of vital importance that researchers continue studies in pursuit of a more complete understanding of this phenomenon.

2.1.3 Turbulent Mixing

The combination of the vorticity imparted by the passing shock wave and perturbation growth due to the RMI leads to turbulent mixing at late times. This turbulence is diffusive, and enhances the transport and mixing of mass, momentum, or a scalar contaminant. Turbulence is also dissipative, and actively removes kinetic energy and scalar fluctuations through dissipation and molecular mixing. Three stages have commonly been used to describe the processes that lead to a state of turbulent mixing [27]: entrainment, stirring, and molecular mixing. Unmixed fluid will first become entrained in the mixing region by large-scale, coherent eddies [12]. The motion of these eddies will stir the fluid, increase the surface area between the different species, and amplify concentration gradients. The sharpening of gradients will enhance viscous and diffusive forces, leading to turbulent dissipation and molecular mixing.

With turbulence comes an inherent distribution and separation of scales occuring in the flow, from the large, energy-containing scale to the small, viscous-dominated scale. The idea of this range of scales and their relationship to one another was first put forward by Richardson [68] as an energy cascade, where eddies break apart to form smaller eddies. This process continues until the eddy is sufficiently small and removed through viscous dissipation. If an eddy has a length scale λ and a velocity scale $u(\lambda)$, then the time scale in which they break apart is related to its timescale, $\tau \equiv \lambda/u(\lambda)$. Breaking apart is equivalent to transferring energy to the next smallest scale, and the rate of this is related to the kinetic energy of the eddy, $u^2(\lambda)$, divided by its timescale. If energy is introduced at the largest scales with an eddy size λ_0, and isn't removed until dissipation at the smallest scale, then an equilibrium develops and the transfer of energy is the same at each scale and equivalent to the viscous dissipation, $\varepsilon = u_0^3/\lambda_0$. This implies that viscous dissipation is independent of viscosity, ν.

With this understanding of energy being produced at the large scale and cascading down an inertial range before being removed through viscous dissipation, one can define two length-scales that separate these very different regimes. At the larger scale, the Liepmann-Taylor scale (λ_L) bounds the isotropic region from the energy-containing range. The Liepmann-Taylor scale is an upper limit of the inertial range, and is interpreted as the smallest scale generated by the largest eddies. The smaller lengthscale, the inner viscous scale (λ_v) bounds the dissipation region and can be estimated as the scale at which the energy spectrum will deviate from the power-law behavior indicative of the inertial subrange regime. Mixing is expected when $\lambda_L > \lambda_v$, and in steady-state flows these scales are related to the Reynolds number through

$$\lambda_L = 5\mathcal{L}Re^{-1/2} \tag{2.16}$$

$$\lambda_v = 50\mathcal{L}Re^{-3/4}, \tag{2.17}$$

where $\mathcal{L}$ is the largest scale of the flow. This implies a transition Reynolds number of $Re = 1 - 2 \times 10^4$, which has been supported by experimental observations [27, 85].

2.2 Motivation

The broader impacts of the RMI are numerous and wide-ranging. At the largest of time and length scales, the RMI presents itself during the supernova explosion of a dying star. When going supernova, a shock wave travels through the many gaseous layers of the star, and the RMI is reponsible for the appearance of stellar core elements at earlier-than-predicted times [2]. At the smallest of length and time scales, the RMI manifests itself as a destructive mixing mechanism in inertial confinement fusion (ICF) experiments. When maintaining perfect spherical symmytery is of the upmost importance, the RMI wreaks havoc as the mechanism

for mixing of the deuterium-tritium (DT) fuel and the outer ablator layer, causing contamination of the fuel source and inhibiting thermonuclear burn. The RMI and closely related Rayleigh-Taylor instability (RTI) [64, 73] are thought to be among the most influential causes preventing ignition in ICF. Though viewed as a hindrance for its contribution to mixing in the realm of ICF, this enhanced mixing brought on by the RMI is of great favor in certain aerospace applications. Between the largest and smallest of scales, the RMI plays a crucial role in scramjet engines [45, 87]. Aiding in the mixing of fuel and oxidizer, the RMI may help to ensure a faster, more-complete burn of fuel, allowing for the development and optimization of airbreathing hypersonic vehicles.

Expanding our current knowledge of shock-interface interactions also shows promise for the advancement of fields including atmospheric sonic boom propagation [22] and shock mitigation in foams and bubbly liquids [8, 17, 23]. A more complete understanding of shock-interface interactions may also help to develop and improve procedures used in the medical field, such as in the treatment of gallstones and kidney stones, where a shock wave can be used to break up hardened deposits that occur within various organs [24, 29, 32].

In addition to their possible influence on the numerous fields affected by advancements in our understanding of the RMI (and shock-accelerated inhomogenous flows, in general), the experiments carried out in the present work serve another very important role. In recent years, scientists have supplemented their theortical and experimental knowledge of fluid flow, turbuence and mixing with computer simulations [14, 34, 36, 70]. Through the implementation of high performance computers, modern-day hydrodynamics codes have proven an important tool for aiding in the expansion of our knowledge of the RMI, and now more than ever, experiments play a crucial role in guiding theory, constraining models, and validating computer simulations.

2.3   Previous Work

2.3.1   Theorical Framework

The origins of our understanding of the RMI begin with the Rayleigh-Taylor instability (RTI), which occurs when a heavy fluid is accelerated into a light one or, alternatively, when the light fluid supports the heavy fluid in the presence of gravity. The linearized problem of the RTI was first provided in 1883 by Lord Rayleigh [64], and in 1950 Sir G. I. Taylor used linear theory to show that the initial growth of an interfacial perturbation is linear until its amplitude becomes comparable to its wavelength [73]. After an initial transition period, interface pertur- bations were theorized to evolve to a turbulent mixing region. A theoretical prediction for the RMI was first provided in 1960 [69] when Richtmyer modified Taylor's analysis to describe the evolution of an impulsively-accelerated interface. In particular, he replaced the constant acceleration term in Taylor's analysis with an impulsive one (as detailed in Sec. 2.1.2). In this way, the RMI can be considered the impulsive-acceleration limit of the RTI; however, unlike the RTI, the interface will be RMI unstable regardless of the direction of acceleration.

The impulsive acceleration required for the development of the RMI is typically provided by a passing shock wave. After reshock, where the shock wave reflects off the end wall of the shock tube and interacts again with the interface, further development of existing theortical models was required to describe the evolution of the reshocked-interface. A theoretical model of a reshocked interface was proposed by Mikaelian [50], where he showed the mixing layer grows linearly after reshock and the growth is independent of the pre-shock initial conditions. According to Mikaelian, the mixing-layer thickness after reshock should fit the form

$$h = C_M A^\dagger V_0 t + h_0 \, , \tag{2.18}$$

which extended the RTI growth rate results from [65] and [89] to an impulsive acceleration, and has been shown to fit many experimental results [43, 65, 75, 88]. According to this model, the growth rate is $\dot{h} = C_M A^\dagger V_0$, which is in contrast to the growth rate of a single-mode initial condition, which is proportional to the amplitude-to-wavelength ratio.

While this theoretical work often provides foundational knowledge that guides experimental research, RMI experiments are required to constrain and validate these proposed models describing the evolution of the instability. A large number of RMI experiments have been performed over the past decades, and these shock tube studies conducted by others must be considered for a complete understanding of the importance of the current work in the ongoing investigation of the RMI. A summary of numerous experimental studies is provided in the following section, providing insight into the development of new experimental methods and diagnostics, along with identified challenges and significant results from each group.

2.3.2   Experimental Studies

The first experimental studies providing verification of Richtmyer's theory were conducted in 1969 by E. E. Meshkov [48]. In these experiments, a sinusoidal nitrocellulose membrane was used to separate various gas pairs before acceleration by a shock wave, and the interface was shown to be unstable regardless of whether the shock passed from a heavy gas to a light gas or from a light gas to a heavy gas. First introduced by Meshkov, the use of a membrane to separate test gases is a technique that has been commonly used in many subsequent experiments [41, 49, 76]. In the work of Vetter and Sturtevant [75] a wire mesh was used to support a membrane separating air and SF_6, and the interface was accelerated using shock waves with a strength ranging from $M = 1.2$ to $M = 2.0$ that approached the interface from the air side. In

these experiments, integrated measurements of the mixing layer thickness were obtained using schlieren visualization, and the presence of the membrane and wire mesh was shown to have a significant effect on the growth rate of the interface. Additionally, membrane fragments have been shown to interfere with the flow and can impede certain diagnostic techniques [42, 30].

To address these issues, a number of new methods were developed to eliminate the need for a membrane and wire mesh, allowing for the creation of a membraneless, continuous interface. By the 1990's, experiments had begun using thin, flat, retractable plates in a vertical shock tube to separate two gases in a light-over-heavy configuration [10, 11]. This technique generates a relatively thick, diffuse interface, which has been shown to significantly reduce the growth rate of the mixing layer. Another method of creating a membraneless interface for use as an initial condition to the RMI was developed by Jones and Jacobs [39] at the University of Arizona. Using a vertical shock tube, N_2 was flowed from the top of the tube while SF_6 was flowed from the bottom. At the location where the two gas streams meet, a vacuum slot in the side of the shock tube was used to evacuate excess gas, establishing a gravitationally stable stagnation plane. With the stagnation plane fully developed, the shock tube was then laterally oscillated, imposing a sinusoidal perturbation on the interface. Later experimental work at the University of Arizona continued this membraneless method of interface creation using PLIF diagnostics [15, 37] and showed excellent agreement with incompressible linear stability theory. Of particular interest to the present study are the PIV investigations of the shock-induced single-mode RMI [4, 52], where PIV results are compared to PLIF and Mie scattered images of the interface.

The stagnation plane method of generating a membraneless interface described above paved the way for later work conducted at the University of Wisconsin by Motl et al. [53, 54] to explore a nominally single mode perturbation created using a technique similar to that used

at the University of Arizona. Rather than oscilating the entire shock tube to create the perturbation, as was done in Arizona, Motl employed the use of two opposing pistons (which contained slots for evacuating the gas mixture at the stagnation plane) to impose a standing wave at the Rayleigh-Taylor-stable interface. In Motl's work, the single mode interface was not only created over a wide range of Atwood numbers, but also accelerated at several different Mach numbers to explore the importance of various flow parameters. This parameter study lead the way to later work conducted in the Wisconsin Shock Tube Laboratory by Weber et al. [79, 82]. In these studies, Weber developed a new method of interface creation, allowing for study of a broadband interface comprised of perturbations of varying wavelength and amplitude [81, 85], and the development of the RMI was investigated using PLIF visualization of the mixing layer at four post shock times. This broadband shear layer initial condition (described further in Sec. 3.2) serves as the basis for the investigation of the evolution of velocity and concentration in the present work.

Experiments conducted at Los Alamos National Laboratory (LANL) have also utilized a membraneless interface and planar imaging of the RMI [61, 6], although these studies employ a horizontal shock tube to study the development of a shocked gas curtain. In these studies, the shock tube is filled with air and a downward flowing curtain of SF_6 containing a tracer is accelerated by a shock wave [7, 5, 57]. In this way, the shock wave passes through not one, but two interfaces, differentiating this work from that conducted in vertical shock tubes such as those found at the University of Arizona and the University of Wisconsin. In addition to studies strictly utilizing horizontal or vertical shock tubes, such as in Wisconsin, Arizona and LANL, work at Texas A&M University [46] has focused on the effect of the RMI on an inclined interface. In this facility, a fluid interface can be created at a prescribed angle to the incident shock by tilting the entire shock tube relative to the vertical direction, with inclination

angles of 0°-90°. Planar laser Mie-scattering is used to obtain measurements of the evolving interface before and after reshock, and 2D velocity fields are obtained using PIV. While these studies of the inclined interface RMI are still active today, they are no longer conducted in the Shock Tube and Advanced Mixing Lab of Texas A&M, as the shock tube has been relocated to the Georgia Institute of Technology.

2.3.3 Computational Investigations

In recent years, theoretical and experimental studies of the RMI have been supplemented by computational investigations of the instability. In some of these studies, experimental conditions have been recreated and solved numerically using high-performance computers that employ several different methods of computation. Perhaps one of the most commonly simulated experiments is that of Vetter and Sturtevant [75]. Cohen et al. [14] used these experiments as a basis for numerical simulations, employing simplified piecewise-parabolic method (sPPM) simulations with varying mesh sizes to explore the importance of resolution for computational results. A similar code was used by Grinstein et al. [34] at lower resolutions (up to 1640×4802). Hill et al. [36] used large-eddy simulations (LES) techniques with a fifth-order weighted essentially non-oscillatory (WENO) scheme. Finally, Schilling and Latini [70] used a ninth-order WENO scheme. All of these simulations showed agreement with the experimental post-reshock growth rate, which was found to be relatively insensitive to the resolution of the numerical simulations.

Numerical simulations have also been used to obtain additional turbulence quantities, not currently measured in experiment. In 2013, Weber et al. derived a growth-rate model for an RMI mixing layer given arbitrary but known initial conditions [84]. In this study, the authors

used the initial growth rate and characteristic perturbation wavelength as scaling factors, and the model was shown to collapse the growth-rate curves and predict the peak growth rate factor over a range of Mach numbers, Atwood numbers, adiabatic indices, and narrow-band perturbation spectra. Reese et al. [66] used the high-order hydrodynamics code *Miranda* [18] to numerically investigate the effect that small-scale three-dimensional perturbations will have on a 2D-dominated shocked mixing layer. These simulations used the experiments of Motl [54] as a basis for their investigation, and found that a two-dimensional domain will not be able to accurately represent all aspects of the RMI since, at a minimum, the level of mixing will be under-predicted. Because numerical studies such as these are able to obtain flow quantities not currently measured in experiment, experiments with quantitative flow field measurements inside the mixing layer are still required to validate these types of simulations.

Chapter 3

Experimental Setup

3.1   The WiSTL Facility

Experiments were conducted in the Wisconsin Shock Tube Laboratory (WiSTL). This facility is equipped with a 9.13 m, vertical shock tube comprised of a circular driver section of 47 cm diameter and a square driven section with 25.4 cm sides [1]. The two sections are initially separated by a steel diaphragm, which is burst by overpressurizing the driver, creating a shock wave. This shock wave travels downward into the test section where it interacts with an interface to be described in detail in Sec. 3.2 below. A schematic of the shock tube is shown in Fig. 2.

This shock tube is designed to handle strong shocks, and has a modular construction to allow for a variety of experimental setups. There are three distinct portions of the WiSTL shock tube: the driver section, the diaphragm section, and the driven section. The driver section is the top 2.08 m of the tube, which is separated from two high-pressure boost tanks by a pair of pneumatically-controlled fast-acting valves (FAVs). Prior to each experiment, this portion of the tube is evacuated before being filled to 90% of the 2.5 MPa rupture pressure of the 16 gauge steel diaphragm that separates the driver section from the diaphragm section. To create a shock wave, the FAVs are opened, allowing gas from the boost tanks to flow into the driver section, thus providing the remaining pressure needed to burst the diaphragm and create
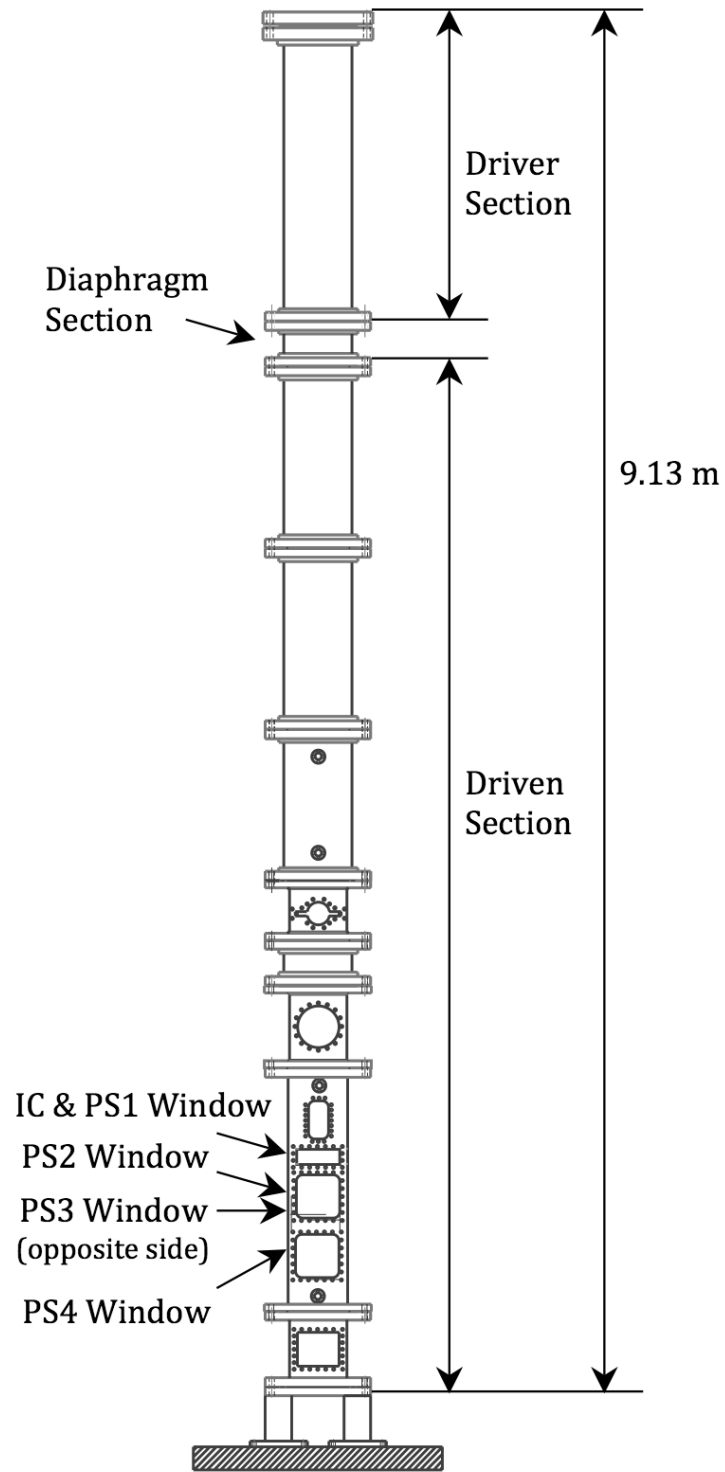
Figure 2: Schematic of the shock tube, adapted from Ref [63].

(a)

(b)

(c)
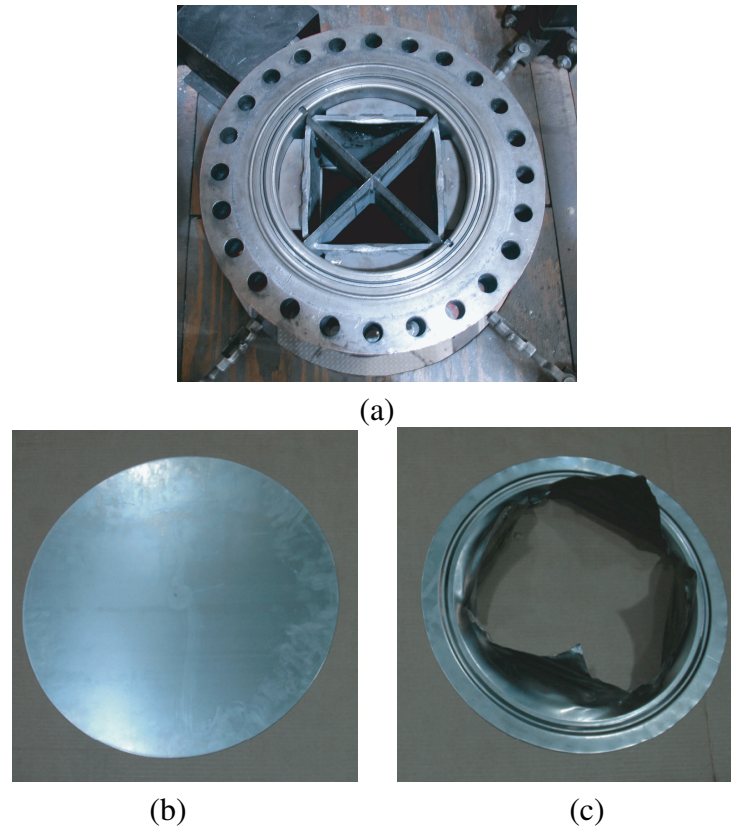
Figure 3: Diaphragm and knife edge for repeatable ruptures. (a) Knife edge used for repeatable ruptures, (b) unused diaphragm, and (c) ruptured diaphragm.

a shock wave.

The next section down is the diaphragm portion of the tube, shown in Fig. 3(a) with the driver removed. This segment is 0.35 m in height, and contains a cross made of sharp, metal knife edges on which the diaphragm sits. The purpose of this section is to ensure that the diaphragm will burst in a repeatable way. The cross forces the diaphragm to rupture with four petals that stay attached to the rest of the diaphragm; this way metal pieces do not travel further downstream, where they can damage the shock tube and chip windows. An image of the diaphragm before and after use is shown in Figs. 3(b) and 3(c), respectively.

Directly under the diaphragm section is the driven section, comprised of the remaining 6.7

m at the bottom of the shock tube. The length of this portion of the tube ensures that the shock wave has sufficient time to develop, and that it is planar by the time it reaches the interface. The sizeable internal cross section of the driven section allows for a large region of the flow to remain unhindered by the boundary layers that form on the side walls. The bottom half of the driven section is the test portion of the tube, where the outer structure of the tube transitions from a circular to a square cylinder to allow for the easy placement of windows, gas injectors, vacuum lines, and any other tube-mounted apparati.

Embedded within the inner walls of the driven section are 12 piezoelectric pressure transducers placed along the length of the tube that are used to collect pressure readings as well as trigger the cameras and lasers used for diagnostics. There are also seven openings in the driven section that allow for the filling and evacuating of gases: heavy gas fill inlet at the bottom, heavy gas injection at the slots, heavy gas particle seeding port below the interface, light gas injection at the slots, light gas particle seeding port above the interface, light gas fill inlet at the top, and vacuum opposite the slots.

3.2   Initial Condition

Creating the initial condition used in the present work is a multi-step process that begins by evacuating the driver and driven sections to a pressure below 17 kPa in order to remove air and any other gas impurities from the shock tube. A gravitationally stable stagnation plane is then created by flowing a light gas from the top of the tube and a heavy gas from the bottom while continuously evacuating excess gas through slits on the tube wall at the interface location. This flow is maintained for several minutes to ensure that all remaining air and impurities have been cleared from the tube.
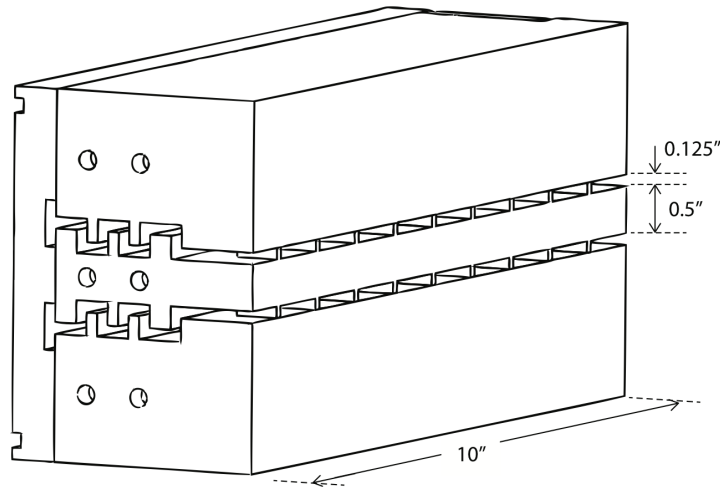
Figure 4: Schematic of the slots used to create the initial condition, taken from Ref [79].

After the stagnation plane has stabilized, a statistically repeatable, broadband, shear layer initial condition [79, 81] is set up by injecting each gas through slots located on the shock tube side wall at the interface, 2 m above the bottom of the tube. A schematic of the slots used to create the initial condition can be seen in Fig. 4. The light gas is flowed from the bottom set of slots while the heavy gas is flowed at a higher rate from the top set of slots, and this mismatch of flowrates establishes the shear layer.

There are a number of important properties of this interface that are to be considered. First, we note that this method of slot-injection from the shock tube side wall creates a three-dimensional shear layer that can never be identically reproduced. However, introduced and characterized by Weber et al. [79], this initial condition has been shown to be statistically repeatable in terms of spectral content, as well as provide a reliable method of creating a membraneless interface containing a large range of scales [81]. A summary of important gas properties (including post-shock interface velocities, wave speeds, temperatures, densities, and Atwood numbers) for the two Mach number cases considered in the present studies is

Table 1: Gas properties for the two Mach number cases. Daggers denote post-shock quantities. Gas 1 is the light gas (helium seeded with acetone) and gas 2 is the heavy gas (argon). V_0 is the post-shock interface velocity.

M_i	1.6	2.2
M_t	1.9	2.9
W_i (m/s)	1150	1576
W_t (m/s)	592	919
V_0 (m/s)	315	606
Acetone (% Vol.)	7	7
ρ_1 (kg/m^3)	0.3	0.3
ρ_2 (kg/m^3)	1.6	1.6
$\rho_1^\dagger$ (kg/m^3)	0.7	1.2
$\rho_2^\dagger$ (kg/m^3)	3.5	4.8
$T_1^\dagger$ (K)	497	761
$T_2^\dagger$ (K)	557	1011
$p_1^\dagger = p_2^\dagger$ (MPa)	0.4	1.0
A	0.7	0.7
$A^\dagger$	0.7	0.6
$(1 - V_0/W_i)$	0.7	0.6
$\left(\rho_1/\rho_1^\dagger + \rho_2/\rho_2^\dagger\right)/2$	0.4	0.3

given in Table 1.

Experimental images of the initial condition for PLIF and PIV studies can be seen in Figs. 5(a) and 5(b), respectively. In both images, a light gas and a heavy gas are injected from the slots on the left side of the frame and evacuated from the right, causing flow from left to right. The PLIF initial condition image shows a black region of pure heavy gas at the bottom of the image, and a white region at the top consisting of only the light gas. In between these two regions is the grey shear layer, where the light gas injected from the lower slots mixes with the heavy gas injected from the upper slots. For comparison, the PIV initial condition image (Fig. 5(b)) shows full-field particle seeding obtained by introducing TiO_2 into the regions directly

<center>(a)   (b)</center>
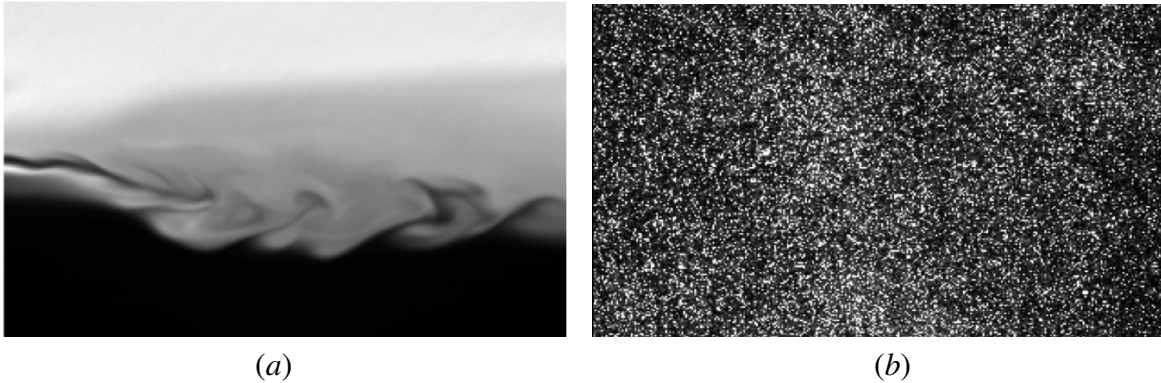
Figure 5: Images of the shear layer initial condition used in the present studies as seen by the (a) PLIF camera, and (b) PIV camera.

above and below the interface, as well as in both horizontal gas injection streams. Details of the experimental setup used to obtain these images are given in the next section.

3.3   Experimental Configuration

With an appreciation for the overall design of the shock tube, as well as an understanding of how the interface is created, we can now focus on the specifics of the experimental configuration used to investigate the RMI. Here, the initial condition and shocked interface are characterized using both the PLIF and PIV methods, and each of these techniques requires its own unique configuration of lasers, optics, and cameras; however, these individual configurations must work together to yield simultaneous concentration and velocity results. A schematic detailing the experimetal setup used for the present studies is shown in Fig. 6.

The first step of the PLIF setup involves molecularly seeding the light gas with acetone. The $\sim 7\%$ acetone vapor concentration used for the experiments described here is achieved by bubbling helium through liquid acetone which is maintained at 308 ± 3 K through the use
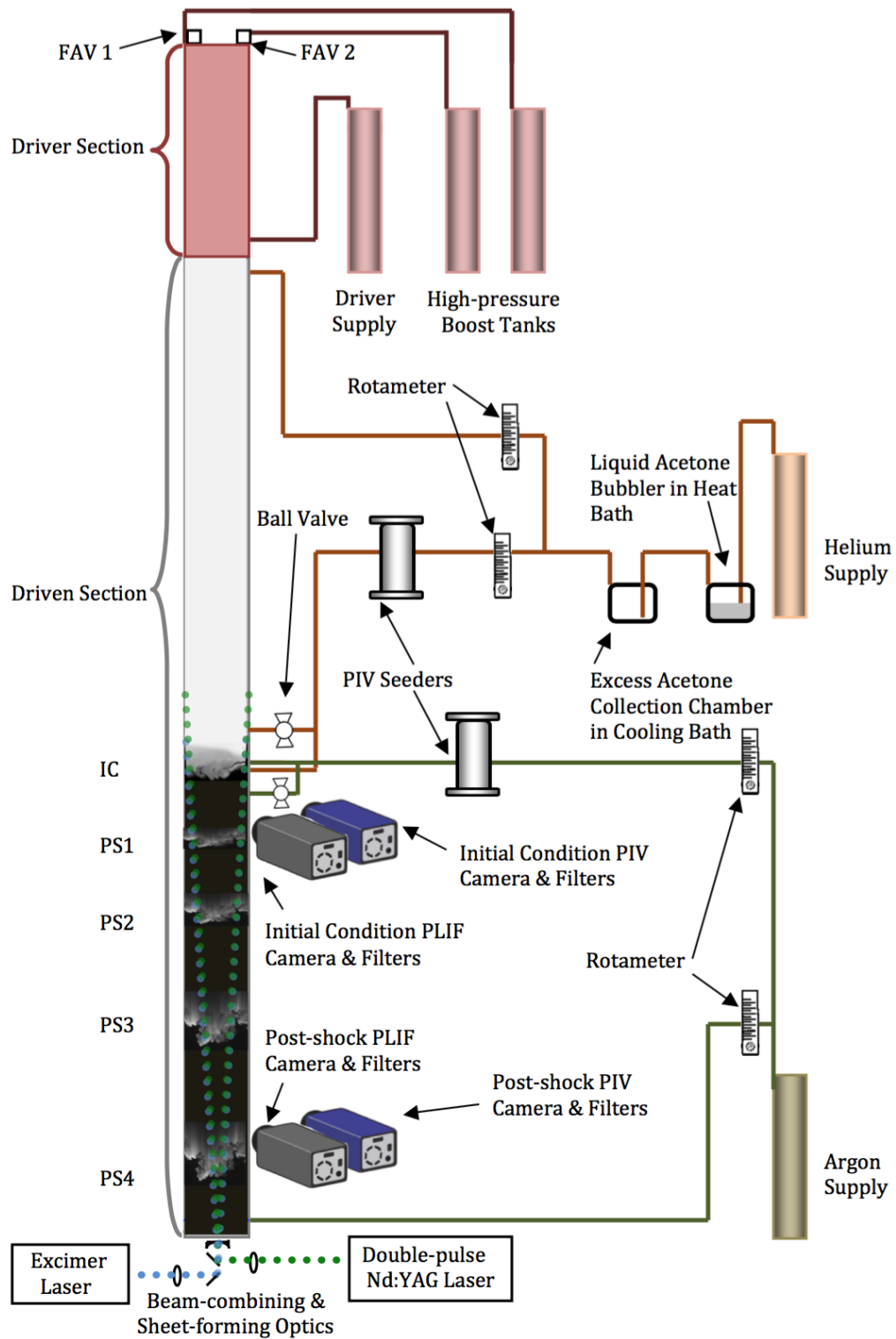
Figure 6: Experimental configuration showing cameras, lasers, optics, plumbing, and molecular & particulate seeding setups used for simultaneous PIV and PLIF experiments.

of a heated water bath. This heavily seeded helium is then flowed through a second container in a cool bath, kept at 283±2 K, in order to bring the acetone concentration down to the desired percentage, well below the saturation level of 24%. Ultraviolet light (308 nm) from a XeCl excimer laser (Lambda Physik LPX 210i) is formed into a sheet and used to excite the acetone present in the helium gas for PLIF imaging. Fluorescence from the acetone is captured on a thermoelectrically cooled (to 218 K) CCD camera (Andor model DV434-BU2), using a 50-mm Nikon lens ($f/\# = 1.2$) with a Schott BG39 filter centered at 470 nm with a full-width half-max of 271 nm, and an ultrasteep short-pass filter only allowing passage of signal below 524 nm. This combination of filters ensures that only fluorescence signal from PLIF is captured by the Andor sensor.

For the PIV measurements, TiO_2 particles with a nominal diameter of 300 nm are seeded into both gas cross-flows used to create the initial condition shear interface, and into the regions immediately above and below the interface. These particles allow for the Mie scattering of the second harmonic output (532 nm) of a dual-head, flashlamp-pumped Nd:YAG laser (Ekspla model NL303D). Using a series of optics, a laser sheet is formed for use in planar laser imaging, and allows for cameras to capture particle images with a ~20×25 cm field of view. Post-shock image pairs are captured with a 29 MP interline image transfer camera (TSI inc. model 630094) using a 4 μs inter-frame time, while initial condition image pairs are taken with the same camera, but using an inter-frame time of 1 ms. The inter-frame times are chosen to compensate for the vastly different interface velocity fluctuations before and after acceleration by the shock wave. These timings also allow for the final search box used in PIV to be reduced in order to obtain a large number of velocity vectors, yielding finer spatial resolution of velocity while maintaining sufficient displacement of the particles.

Because experiments are performed at two different Mach numbers and the post-shock

Table 2: Summary of experimental image times and locations.

	Distance (m) from IC	Time (ms) $M = 1.6$	Time (ms) $M = 2.2$	Number of images
IC	0	0	0	20
PS1	0.05	0.14	0.10	20
PS2	0.27	0.88	0.44	20
PS3	0.67	2.16	1.12	20
PS4	1.21	3.84	2.05	20

interface was captured at the same locations for each case, the timings used to capture the interface in a given window downstream of the initial condition will be different for the two sets of experiments. These distances and timings are summarized in Table 2. Important timings are also shown in the *x-t* diagrams of Fig. 7. In these figures, the leftmost red line shows the contact surface between the driver and the driven gas, while the rightmost red line denotes the interface location. The black line downstream (to the right) of the contact surface represents the shockwave, shown to break into a rightward-traveling transmitted wave and leftward-traveling reflected wave after hitting the interface. The black lines to the left of the contact surface represent an expansion fan, while the light blue bands show the locations of the windows used for imaging the interface throughout the development of the RMI.

3.4   Experimental Error

The thickness of the laser sheet is an important factor in determining experimental error for both PLIF and PIV measurements. Laser sheet thickness as a function of height was determined using a scanning knife edge technique for both the 308 nm excimer laser and the 532 nm Nd:YAG laser, where the relative power of the laser was measured as a razor was traversed
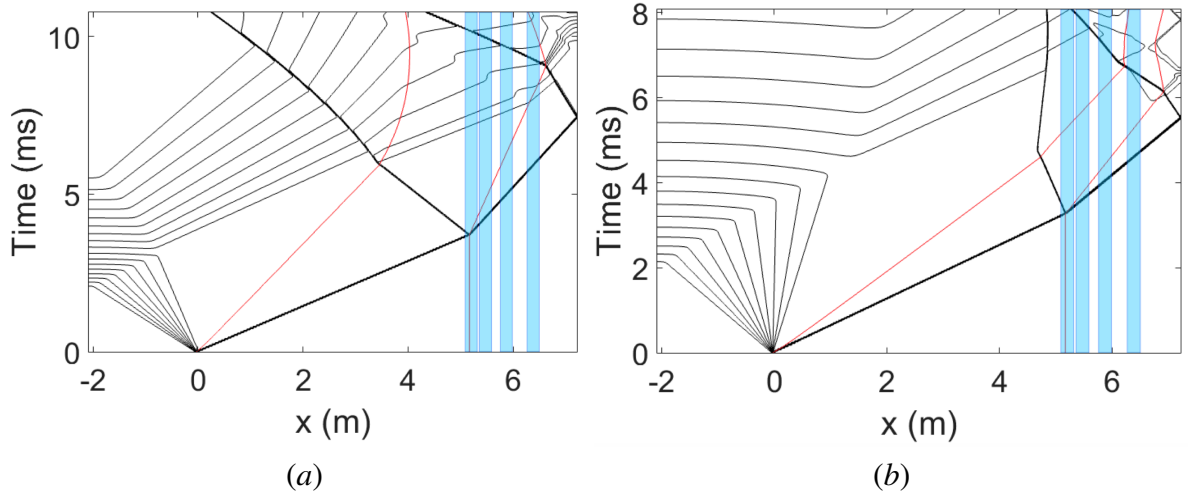
Figure 7: *x-t* diagrams for the (a) $M = 1.6$ and (b) $M = 2.2$ experiments. Rarefaction waves are shown as thin black lines initially propagating leftward (upward) into the driver, while the shock front is shown as the thick black line initially traveling rightward (downward) into the driven section. Light blue bands show the imaging windows, and the right-most red line shows the interface location.

through the sheet. In this way, measurements of the sheet thickness can be made at several downstream locations, and the laser waist can be determined by finding the minimum of the fit over several measurement locations. For PLIF experiments, the laser sheet thickness at the point of imaging was determined to be ~0.7 mm, while a thickness of ~0.5 mm was found for PIV studies. Measurements across the laser sheet at a single downstream location are shown in Fig. 8(a) for the Nd:YAG laser sheet. The circles in Fig. 8(b) represent the half-widths of the 10-90% energy thickness of the sheet [71] as measured from profiles shown in Fig. 8(a) at several location along the height of the beam path. The equation for the propagation of a real (non-Gaussian) laser beam [72] is given by

$$w_b^2(z) = w_{b,0}^2 + \left(M_b^2 \frac{\lambda}{\pi w_{b,0}} \right)^2 (z - z_0)^2,$$
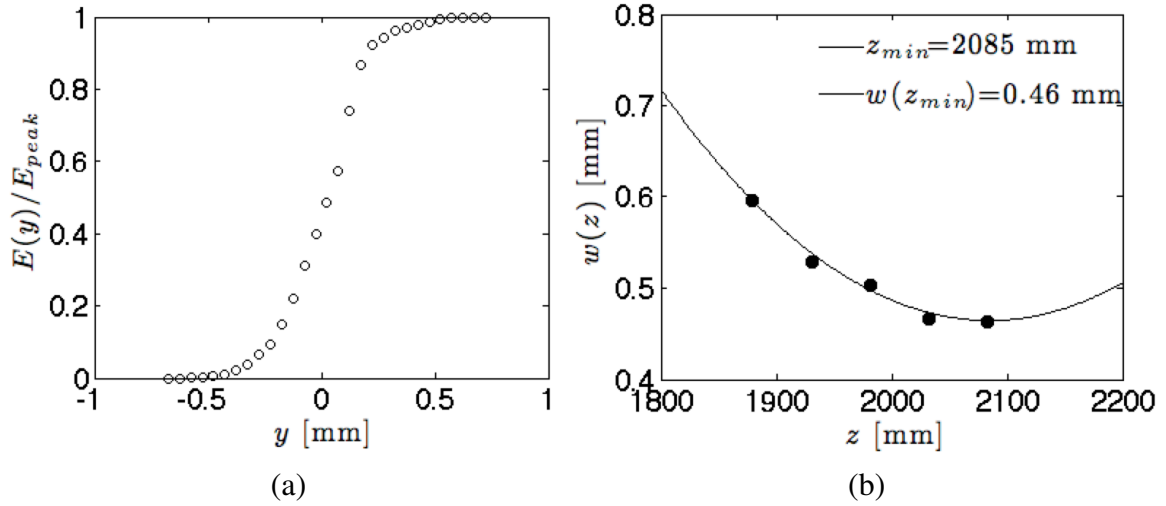
(3.1)

Figure 8: Thickness measurements of the 532 nm laser sheet using scanning knife edge method and a 2 m focal length spherical lens. (a) Cumulative power vs. razor blade traversal, and (b) beam waist vs. beam path distance (as measured from the location of the spherical lens).

where w_b is the beam waist, λ is the wavelength of light, and M_b^2 accounts for the beam's departure from a Gaussian profile. By fitting the measured beam waists, values of $w_{b,0} = 0.46$ mm, $z_0 = 2085$ mm, and $M_b^2 = 5.2$ are found for the Nd:YAG laser, and values of $w_{b,0} = 0.72$ mm, $z_0 = 2206$ mm, and $M_b^2 = 72$ are found for the excimer laser. The high M_b^2 value of the 308 nm laser is expected due to the non-Gaussian profile typical of excimer beams.

Although one should work to obtain the thinnest sheet possible for PLIF imaging (in order to avoid obtaining an integrated signal over the entire thickness of the laser sheet), there is an advantage to having a finite thickness in the laser sheet for PIV. Because velocity is three dimensional, any out-of-plane velocity will not be captured. In the case of PIV measurements, this corresponds to a particle moving out of the imaging plane, and thus being unable to be correlated between images. Using the measured thickness of the sheet used for PIV studies, as well as the timing between sucessive images, we find that a particle centered in the laser sheet

would need to be moving at several hundred m/s in the y-direction in order to escape the laser sheet. Since this velocity is much higher than any velocity-fluctuations measured in the $x-$ or $z-$directions, out-of-plane particle motion should have a negligible influence on velocity measurements.

Chapter 4

Data Processing

4.1 Concentration from PLIF

Prior to processing the PLIF images to reveal mole fraction, the background signal is subtracted from each raw image. The background signal is an ensemble average of 10 images with the same optical setup, including laser pulses, but with no acetone in the field of view. This background image contains both the camera noise and light scattered off the walls of the shock tube. A second background subtraction step is then applied, subtracting the average intensity in the unseeded portion of the flow (*i.e.* the lower portion of the image). This ensures that the unseeded portion of the flow has an average intensity of zero. Analytically, this procedure is

$$S_{i,j}^{f,temp} = I_{i,j}^{raw} - \langle I_{i,j,k}^{bg} \rangle_k \,, \tag{4.1}$$

$$S_{i,j}^{f} = S_{i,j}^{f,temp} - \langle S_{i,j}^{f,temp} \rangle_{i,j \in \{unseeded\}} \,, \tag{4.2}$$

where angle brackets denote averaging over the subscript, k is the background image number, {unseeded} is the rows and columns of the unseeded region of the image, and S^f is the final fluorescence signal. Equation (4.1) is an element-wise subtraction of a matrix and Eq. (4.2) is a subtraction of a constant value.

Next, the background-subtracted PLIF images are processed to extract the light-gas mole fraction, ξ, by correcting for non-uniform laser profile, laser sheet divergence, and Beer's law

attenuation. First, the background-subtracted PLIF image is transformed to an $r - \theta$ coordinate system aligned with the laser beam and is corrected for the signal decrease from laser sheet divergence. Then a region in the top portion of the image is selected where a uniform concentration of pure seeded (light, $\xi = 1$) gas exists. The Beer's law attenuation coefficient is determined from this region, corresponding to the acetone absorption cross section. The normalized acetone concentration can then be computed [16] by integrating downward while accounting for the divergence of the laser sheet, such that deviations from Beer's law attenuation are attributed to mixing of unseeded (heavy) gas or changes in temperature. The equation for this is

$$\xi = \frac{\dfrac{T}{T_1} S^f}{S^{f,R} - n_1 \sigma \phi \displaystyle\int_r^R \frac{S^f}{\phi} dr}, \tag{4.3}$$

where S^f is the local fluorescence signal, $S^{f,R}$ is the fluorescence signal at the top of the image where it is assumed $\xi = 1$, T/T_1 is the temperature ratio in relation to the pure seeded region, $n_1 \sigma$ is the product of number density and absorption cross section in the pure seeded gas (this product is measured by the exponential signal variation in the top of the image), and ϕ is the fluorescence quantum yield. The integral is carried out from the location r to the top of the image at location R. This process is similar to that used by Weber et al. [85]. It should be noted that temperature is approximated as

$$T = T_2^\dagger + (T_1^\ddagger - T_2^\dagger)\xi, \tag{4.4}$$

where $T_1^\ddagger$ and $T_2^\dagger$ are the post-shock temperatures in the pure light and heavy gases, respectively, calculated from 1D gas dynamics.

Once concentration has been determined from fluorescence signal as described in equation 4.3, the concentration field is then mapped back into the $x - z$ coordinate system. Finally, the

2D Fourier transform of the corrected image is computed and the spectrum is notch filtered to remove index of refraction artifacts that appear during the image processing proceedure [83]. Following the notch filtering, the inverse tranform of the corrected spectrum is computed and a final concentration field is obtained for each experiment. A representative raw PLIF image is shown in Fig. 9(a), and the corresponding processed image showing concentration is shown in Fig. 9(b). In the corrected PLIF image, white indicates pure light gas, black corresponds to pure heavy fluid, and gray regions represent mixed gas of various species concentration.

4.2 Velocity from PIV

The concept behind obtaining velocity from PIV particle image pairs is simple: with a known time between images Δt, if a group of particles from image one is advected to a different location in image two and the spatial displacement of that group of particles $\Delta \mathbf{x}(\mathbf{x}, t)$ can be determined, the velocity $\mathbf{u}(\mathbf{x}, t)$ for that small search region is estimated using

$$\mathbf{u}(\mathbf{x}, t) = \frac{\Delta \mathbf{x}(\mathbf{x}, t)}{\Delta t} . \tag{4.5}$$

In the present experiments, the most-likely displacement vector of particle groups is determined through spatial correlation analysis of the experimental particle image pairs using the Insight 4G PIV software package from TSI Inc.

For each of the 20 concentration images obtained at every post-shock time, a corresponding particle image pair is captured by the PIV camera such that each pixel is ~50 μm in the focal plane. A single raw particle image is shown in Fig. 9(d). Similarly to processing PLIF images, the first step in obtaining velocity from PIV image pairs is subtracting the background signal from each raw image. Here the background signal for the first particle image is an
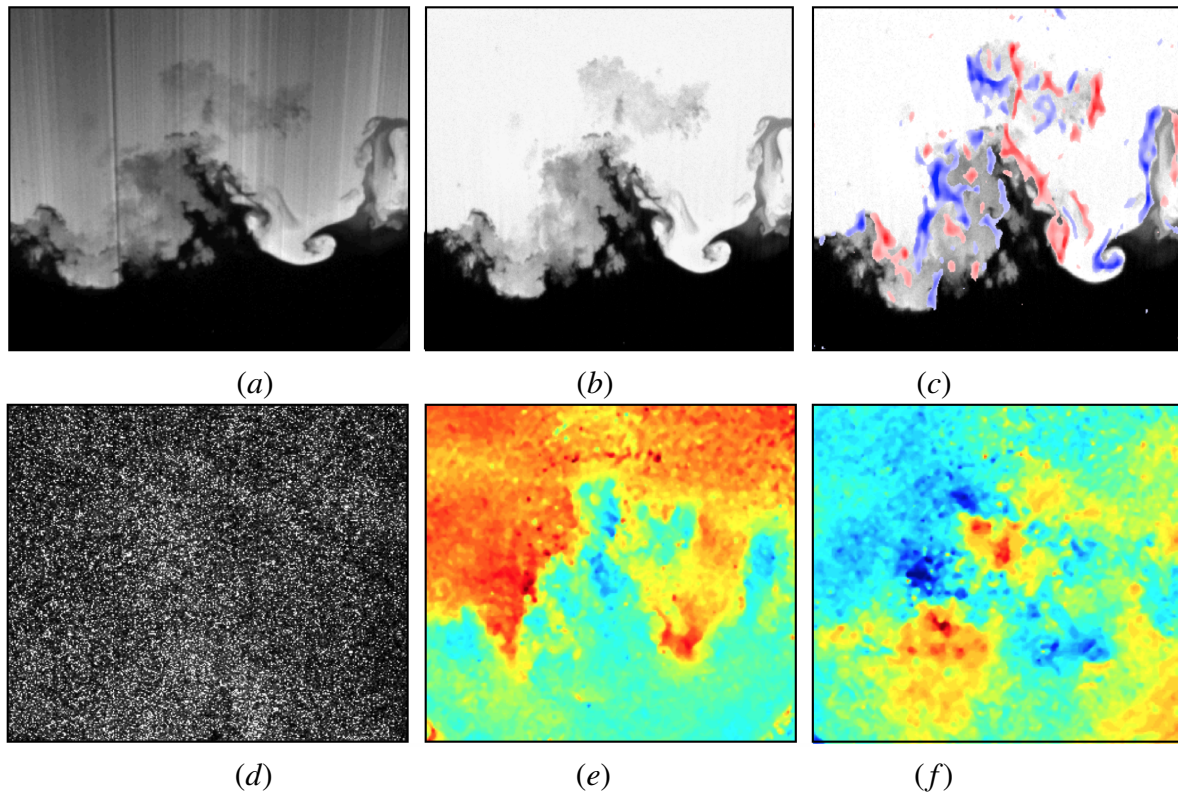
Figure 9: Representative data processing results and field matching for PLIF and PIV. (a) Raw fluorescence signal, (b) corrected PLIF image showing concentration with white indicating pure light gas and black corresponding to pure heavy fluid, (c) vorticity overlaid on ξ field to show field matching, (d) raw PIV particle image, (e) output streamwise velocity with red indicating downward-moving gas and blue corresponding to upward-traveling fluid, and (f) output transverse velocity with red indicating rightward-moving gas and blue corresponding to leftward-traveling fluid.

ensemble average of 10 first-frame images, while the background signal for the second particle image of the pair is an ensemble average of 10 second-frame images. As with PLIF, all background images use the same optical setup, including laser pulses, and contain both the camera noise and light scattered off the walls of the shock tube; however, no TiO_2 particles are present in the field of view for PIV background images. It is this background-subtracted particle image pair that is used as input to the Insight 4G PIV algorithm.

Before conducting cross correlation, a 5×5 Gaussian filter with $\sigma = 0.5$ is applied to background-subtracted image pairs. Following this pre-processing step, a recursive Nyquist grid is used to break the input images into smaller spots for processing, and the first processing pass computes the vector field at a starting spot size of 128×128 pixels with 50% overlap grid spacing. The results of this first processing pass are then used to optimize the spot offsets for the second pass, where the spot size is reduced by a factor of two. This optimization and spot-size reduction occur once more so that a final spot size of 32×32 pixels is achieved. At each pass, a zero pad mask is applied to compute the average pixel intensity of each spot and subtract it from each pixel prior to passing the spots to the correlation engine. This zero pad mask is chosen to increase the signal-to-noise ratio of correlations.

A direct correlator is used to compute the correlation function of the masked spots and return the result as a correlation map. The correlation is computed by first determining the mean intensity in the sample box of image one,

$$\bar{I}_a = \frac{1}{B_x B_y} \sum_{k=1}^{B_x} \sum_{l=1}^{B_y} I_a(k, l) , \tag{4.6}$$

and the mean intensity of the current test box in image two,

$$\bar{I}_b = \frac{1}{B_x B_y} \sum_{k=1}^{B_x} \sum_{l=1}^{B_y} I_b(k + i, l + j) , \tag{4.7}$$

where $I_a(1, 1)$ and $I_b(1, 1)$ represent the pixel intensities at the corner of a pattern box of size B_x by B_y, centered at image coordinates (x,y), in images 1 and 2, respectively. This spot mean intensity is then subtracted from each pixel, and the product of intensities at each pixel offset is summed to give the correlation map. This correlation map is adjusted by an autocorrelation factor to increase the displacement measurement accuracy, giving the variance normalized correlation, or covariance $c(i, j)$, defined by

$$c(i, j) = \frac{\sum_{k=1}^{B_x} \sum_{l=1}^{B_y} (I_a(k, l) - \bar{I}_a)(I_b(k + i, l + j) - \bar{I}_b)}{[\sum_{k=1}^{B_x} \sum_{l=1}^{B_y} (I_a(k, l) - \bar{I}_a)^2 \sum_{k=1}^{B_x} \sum_{l=1}^{B_y} (I_b(k + i, l + j) - \bar{I}_b)^2]^{1/2}} . \tag{4.8}$$

The highest peak in this correlation map is used to locate the particle image displacement, and is determined using a Gaussian peak engine. The Gaussian peak engine locates the correlation peak with sub-pixel accuracy by fitting a Gaussian curve to the highest pixel and its four nearest neighbors. Two 3-point fits are done: one in the x direction with the peak pixel and the pixels to the left and right of the peak, and one in the z direction with the peak pixel and the pixels above and below the peak. The Gaussian peak equation is given by

$$dx = x + \frac{log(l) - log(r)}{2[log(l) + log(r) - 2log(c)]} - x_0 , \tag{4.9}$$

where l, r, and c are the intensity value for the left, right, and peak pixels in the correlation map, x is the integer shift, and x_0 is the zero shift location.

With the x and z displacements determined by Insight, full-field transverse and streamwise velocity can be easily determined using Eq. (4.5) with the known inter-frame time between particle images. Velocity results are then post-processed to remove outliers using a global validation and a 5×5 pixel local test to replace velocity values outside 3σ with the local median. Typical velocity results for the streamwise and transverse directions are shown in Figs. 9(e) and 9(f), respectively. Figure 9(e) shows streamwise velocity, with downward-traveling

regions in red and upward-moving fluid in blue. Comparison with Fig. 9(b) shows that regions of upward-going gas correspond to spikes and downward-moving regions correspond to bubbles in the interface structure. Figure 9(f) shows transverse velocity, with rightward-traveling gas in red and leftward-moving fluid in blue.

4.3   Field Matching

With concentration and velocity fields determined from the raw PLIF and PIV images as described in the previous two sections, the velocity results determined by Insight 4G must now be matched to the corrected ξ field coordinate system. This is accomplished using images of a test target taken prior to each experiment by both the PLIF and PIV cameras to determine the transformation matrix $\mathcal{T}$ that will map the PIV target coordinates $(x, \mathfrak{z})$ to the PLIF target (and ξ field) coordinates (x, z) as

$$[x \ \ z] = [x \ \ \mathfrak{z} \ \ 1]\mathcal{T}. \tag{4.10}$$

Because both cameras' lines of sight are perpendicular to the imaging plane with an overlapping region of interest, the transformation to map the PIV target image to the concentration field need only include rotation, scaling, and a two-dimensional translation, such that

$$\mathcal{T} = \begin{bmatrix} \mathfrak{s}\cos(\Theta) & -\mathfrak{s}\sin(\Theta) & 0 \\ \mathfrak{s}\sin(\Theta) & \mathfrak{s}\cos(\Theta) & 0 \\ T_x & T_z & 1 \end{bmatrix}, \tag{4.11}$$

where $\mathfrak{s}$ is the scale factor, Θ is the rotation angle, T_x is the x-direction translation, and T_z is the z-direction translation. Target images are used to determine the four unknown parameters in Eq. (4.11) by using control points to determine the geometric transformation $\mathcal{T}$. A sample target image from the PIV camera is shown in Fig. 10(c) with four control points selected;

the corresponding control points are then selected on the target image from the PLIF camera, shown in Fig. 10(d). In this way, one can ascertain the transformation variables required to match the control points selected in the $(\mathfrak{x}, \mathfrak{z})$ coordinate system (Fig. 10(c)) with the control points in the (x, z) coordinate system (Fig. 10(d)). With the transformation variables determined in this way, $\mathcal{T}$ can be applied to the TSI target image to account for rotation, scaling, and two-dimensional translation. This transformed PIV target image is shown in Fig. 10(e), and should be compared against the corresponding PLIF target image in Fig. 10(f).

Before applying the determined transformation to velocity fields, velocity output from Insight 4G (Fig. 10(a)) must first be resized to match the PIV target image. Since the final search box used to determine velocity from the PIV particle image pair was 32×32 pixels with 50% overlap, this means that for each 16×16 pixel region in the PIV target image, there will only be a single pixel in the corresponding velocity field. Hence, prior to applying $\mathcal{T}$, velocity fields are first up-sampled using a bi-cubic interpolation where the output pixel value is a weighted average of pixels in the nearest 4×4 neighborhood. This upsampled velocity field is shown in Fig. 10(b). Finally, because the two cameras' sensors had different aspect ratios, the transformed velocity field must also be cropped to the same 1024×1024 size as the ξ field. By cropping the transformed velocity results, each pixel in the $u(x, z)$ and $w(x, z)$ field will match directly to a corresponding pixel in the $\xi(x, z)$ field. This transformed and cropped streamwise velocity field is shown in Fig. 10(g) and should be compared against the corresponding PLIF image in Fig. 10(h) to show the matched features between these fields in the proper coordinate system.

The effectiveness of this matching technique can be seen by overlaying the transformed velocity results on the concentration field. This is demonstrated by first computing the vorticity from velocity fields, $\omega \equiv \nabla \times \mathbf{u}$, and overlaying vorticity above a certain threshold on the
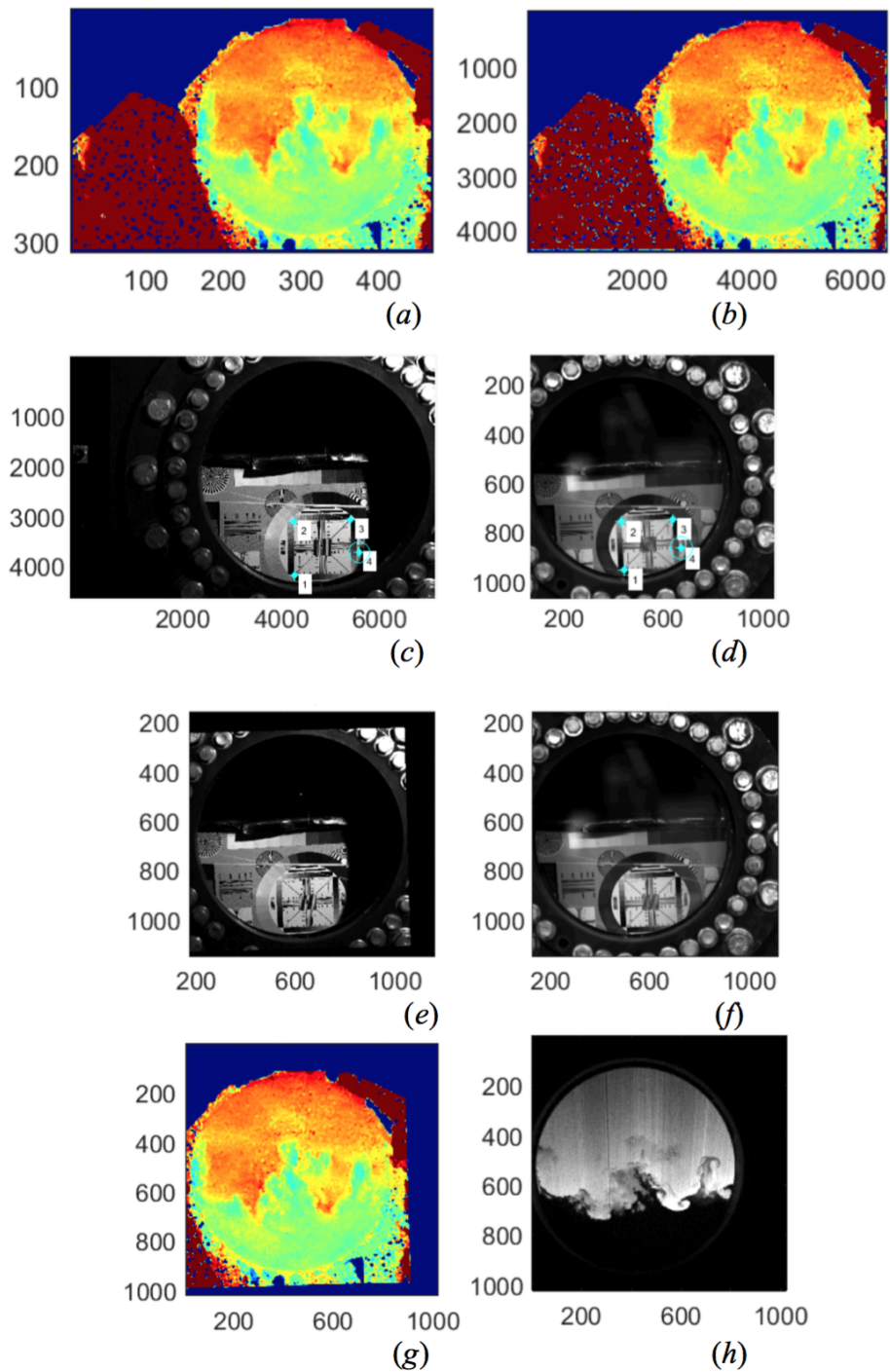
Figure 10: Image registration between velocity and concentration results. (a) Velocity data output from Insight, (b) upsampled velocity field matching resolution of PIV target image, (c) PIV target image showing control points, (d) PLIF target image showing control points, (e) registered PIV target image, (f) PLIF target image, (g) registered velocity field matching PLIF image, and (h) raw PLIF image.

corresponding ξ field, as shown in Fig. 9(c). Here we see that, as expected, the regions of strongest vorticity correspond directly to those locations of concentration that have the strongest gradients. Moreover, by visualizing the vorticity of the gas within the mixing zone, further insight into the effect of velocity on interface structure can be easily obtained.

4.4 Decomposition of Fields

The first step in determining velocity fluctuations in the flow is to subtract the field average velocity from each pixel. For the streamwise direction, this subtraction accounts for the post-shock interface velocity, and is near the 1D gas dynamics value of the flow (~315 m/s for $M = 1.6$, and ~605 m/s for $M = 2.2$), such that

$$\hat{w} = w - w_{avg}, \tag{4.12}$$

where w is the measured velocity field, w_{avg} is a single value representing a global field average velocity, and $\hat{w}$ is the mean-subtracted velocity field which will be referred to as the global fluctuations. This $\hat{w}$ field has a velocity distribution centered about 0 m/s, and shows the large-scale structure of the streamwise velocity. An example of a mean-subtracted velocity field is shown in Fig. 11(a). The same process is also carried out for the transverse velocity field.

With the global fluctuation fields determined from Eq. (4.12), the flow can now be further decomposed into a mean field and a local fluctuation field. Two different methods were applied to achieve this decomposition, and each was applied to both the concentration and velocity fields so that

$$\hat{\mathbf{u}} = \overline{\mathbf{u}} + \mathbf{u}' \quad \text{and} \quad \xi = \overline{\xi} + \xi', \tag{4.13}$$
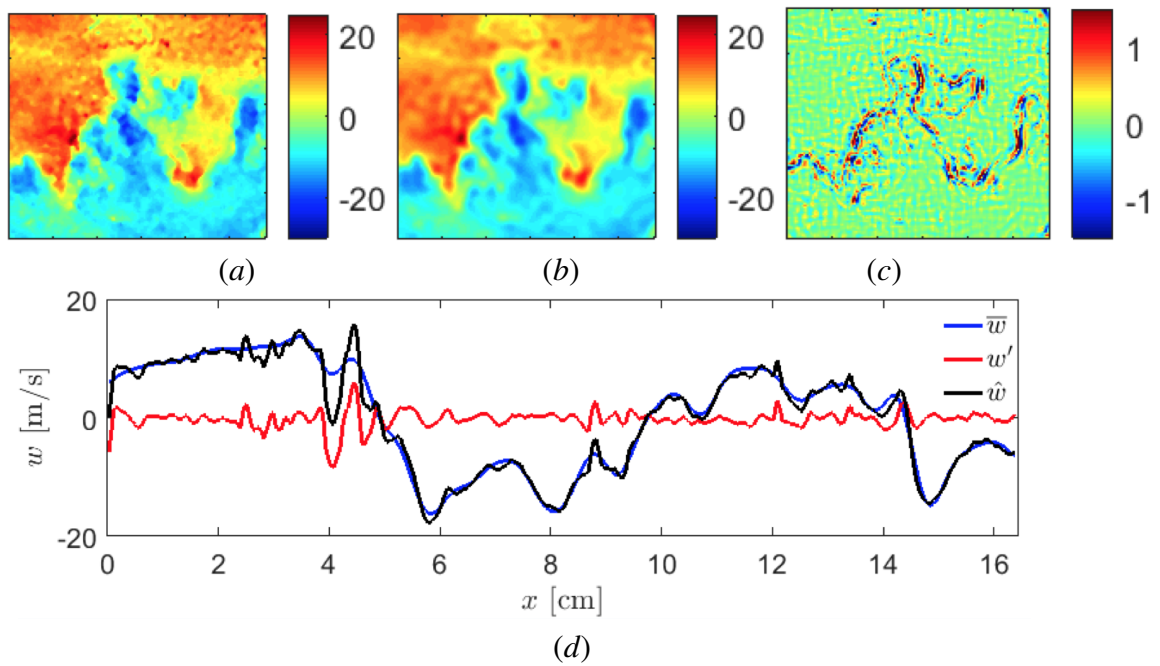
Figure 11: Field decomposition showing the (a) global-mean-subtracted field $\hat{w}$, (b) mean field $\overline{w}$, (c) fluctuation field w', and (d) line plots showing the breakdown into mean and fluctuations through the mixing layer. Line plots in (d) are taken from the center row. Colorbars in (a)-(c) are in m/s.

where an overbar indicates the mean field, and a prime denotes the fluctuating field which will be referred to as the local fluctuations. Ideally, one would ensemble average results over several experiments to obtain a mean flow field; however, the run-to-run variation of the fields proved too great to give meaningful results using this method. Instead, the first technique we will explore to determine this decomposition involves using a two-dimensional moving boxcar average to calculate a mean component of concentration and velocity for each experiment, while the second method utilizes spectral filtering to remove small-wavenumber features from the fields.

The mean flow field was first obtained for each experiment by filtering the concentration and velocity global fluctuation fields with a 2D moving boxcar average. Of course, since this method of filtering utilizes a set window size over which averaging occurs, the size of the filtering window should be based on some macroscopic feature of the flow to account for the growth of the mixing layer thickness over time. Here, the filter window size was chosen to be 1/20 of the campaign-average height of the $0.05 < \langle \xi \rangle < 0.95$ region of the mixing layer. In this way, as the number of pixels over which the average is being calculated increases, the boxcar average window grows proportionally. After applying this filter to the concentration and global-fluctuation velocity fields to obtain the mean component of the flow, results were subtracted from the ξ and $\hat{\mathbf{u}}$ fields to yield the local fluctuation fields.

A spectral method was also used to determine the decomposition of concentration and velocity fields. For this method, a two-dimensional fast Fourier transform (FFT) is performed on the field before applying a Fermi-Dirac soft cutoff filter [35], which was constructed as

$$\frac{1}{1 + \exp\left(\dfrac{k_{xz} - k_c}{0.1 k_c}\right)}, \tag{4.14}$$

where $k_{xz} = \sqrt{k_x^2 + k_z^2}$ is the two-dimensional wavenumber, and $k_c = (2\pi)/L_c$ is the cutoff

wavenumber with L_c being the cutoff lengthscale. The filter gradually sets the Fourier coefficients above k_c to zero. The Liepmann-Taylor scale, defined by Grinstein [33] as $\lambda_L = 2.17\lambda_T$ (where λ_T is the Taylor microscale), makes a natural cutoff lengthscale as λ_L represents the smallest scale generated by the largest eddies. In other words, the Liepmann-Taylor scale bounds the isotropic region from the energy containing range (*i.e.* is an upper limit of the inertial range). Finally, the two-dimensional inverse fast Fourier transform (IFFT) is applied to obtain a low-pass (or spatially averaged) field. As with the moving boxcar method, this average field is subtracted from the ξ or $\hat{\mathbf{u}}$ field to obtain the local fluctuation field. Results using this spectral method showed good agreement with results using the boxcar method.

Field decomposition results are shown in Fig. 11 for the streamwise component of velocity using the spectral method of filtering. Figure 11(a) shows the $\hat{w}$ global fluctuation field, and Figs. 11(b) and 11(c) show the corresponding mean $\overline{w}$ and local fluctuation field w', respectively. We note that Fig. 11(c) shows large fluctuations embedded in underlying smaller random fluctuations, and that the regions of strongest fluctuations correspond with the regions of highest vorticity, as shown in Fig. 9(c), which in turn correspond to the regions of largest gradient in the ξ field. A line plot from the center row of each velocity component field is shown in Fig. 11(d), where the black line shows the global fluctuation, the blue line shows the mean component of velocity, and the red line shows the local fluctuating component of the flow.

Chapter 5

Results and Discussion

5.1   Field Structure and Distribution

With the concentration and velocity fields now matched and decomposed using methods dis-
cussed in Chapter 4, this chapter presents results and a detailed discussion regarding the phys-
ical significance of these findings. The structure of the concentration, velocity, and vorticity
fields is discussed in detail, and the distribution of these quantities is explored using probabil-
ity density functions (PDFs). The experimental campaign underpinning the results shown here
yielded full-field concentration and velocity results for nearly 200 shocked interfaces; a rep-
resentatitve subset of these fields is shown in Fig. 12 for the $M = 1.6$ experiments and in Fig.
13 for the $M = 2.2$ runs. The leftmost column of these figures shows concentration results,
where white corresponds to pure light gas, black corresponds to areas containing only argon,
and gray indicates regions of mixed fluid. The second column shows the global fluctuation
transverse velocity field, where blue corresponds to leftward-moving gas and red indicates
rightward-going fluid. The third column of Figs. 12 and 13 shows the global fluctuation
streamwise velocity field, with blue indicating upward-moving fluid and downward-traveling
gas shown in red. Finally, the last column shows the vorticity field ω_y (henceforth referred to
simply as ω) calculated from the curl of the velocity. The broadband, shear-layer initial con-
dition is shown in the top row, and post-shock results (PS1-PS4) are shown in the following

four rows. Note the difference in colorbar scaling for velocity and vorticity fields between the initial condition and post-shocked results due to the vastly different velocities within the mixing layer before and after acceleration by the shock wave.

The shear-layer initial condition ξ-field is shown in the first column of the top row of Fig. 12, while the $\hat{u}$ field shows a rightward-moving jet corresponding to the injected gas from the left side of the tube, with recirculation zones developing above and below the injection sight on the left side of the velocity field. The $\hat{w}$ field shows alternating upward and downward traveling gas typical of the Rayleigh-Taylor and Kelvin-Helmholtz intabilities. Due to the horizontal injection of gas used to create the shear layer, vorticity fields for the initial condition show a generally horizontal banding of vorticity across the interface. In the next row down, the PS1 ξ-field shows compression of the interface following passage of shock wave, while $\hat{u}$ shows the beginning of a breakup of the coherent jet seen in the initial condition and $\hat{w}$ shows an intensifying of the alternating upward and downward velocity. There is a continual breakup of the jet and a development of large-scale spike and bubble structures seen at each succesive post-shock time, until coherent spike and bubble structures appear by the latest post-shock time. In the last row of Fig. 12, the effect of velocity on interface structure is evident as regions of strong upward motion correspond with spike features, and downward moving gas aligns perfectly with bubbles in the ξ-field. Vorticity is shown to be strongest along the regions of largest gradients in the ξ-field, and the horizontal banding of ω seen at the initial condition has given way to alternating vertical bands of vorticity aligned with the spike and bubble structures seen at the PS4 time.

Results from the $M = 1.6$ experiments are similar to the higher Mach number case, although there is more turbulent mixing occuring by late times for the $M = 2.2$ case, as evident by the break down to smaller-scale features and more "gray" mixed gas regions in the ξ-fields.
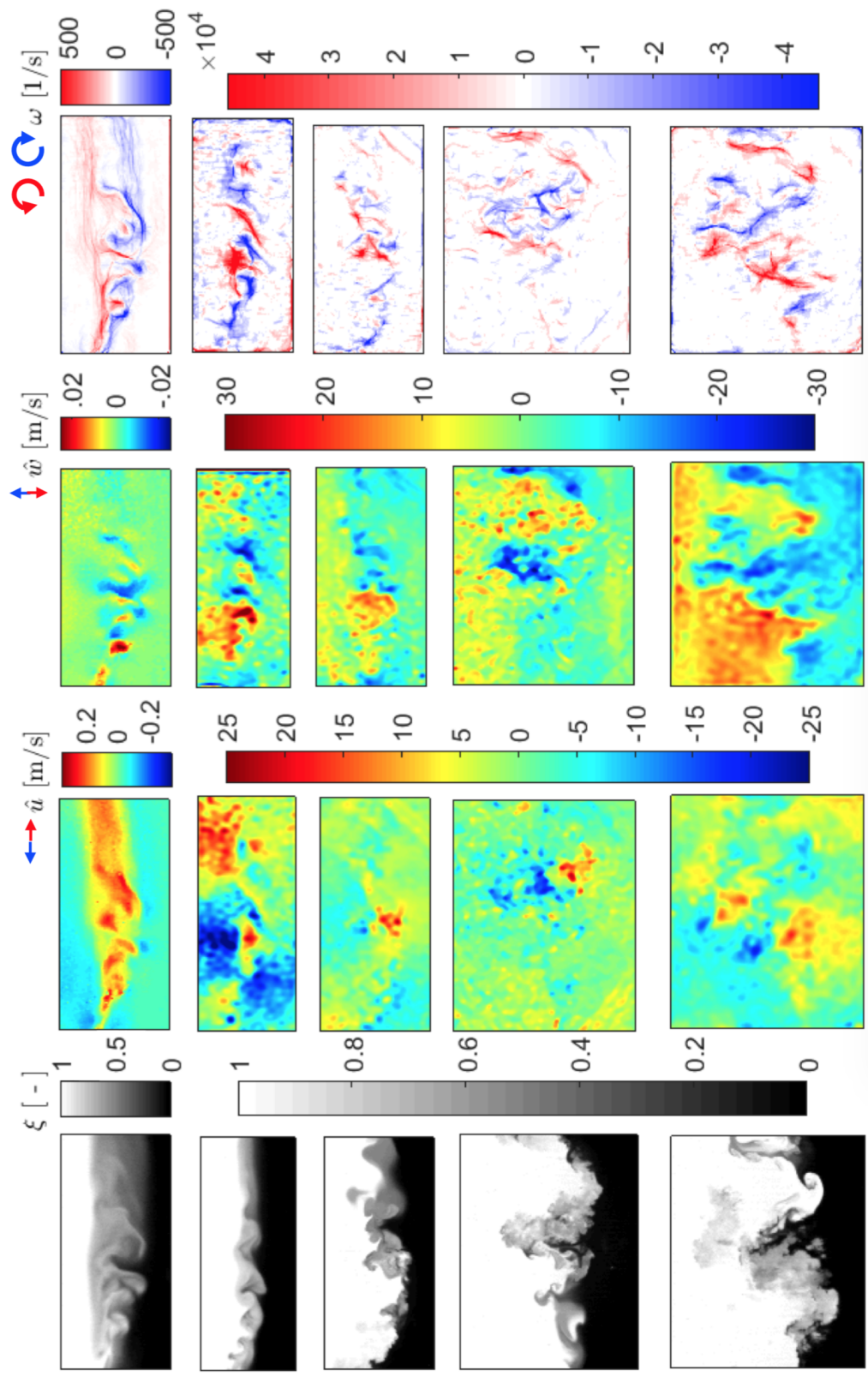
Figure 12: Representative field evolution results for the $M = 1.6$ case. From top to bottom: IC, PS1, PS2, PS3, PS4. From left to right: concentration ξ, global fluctuation transverse velocity $\hat{u}$, global fluctuation streamwise velocity $\hat{w}$, and vorticity ω.
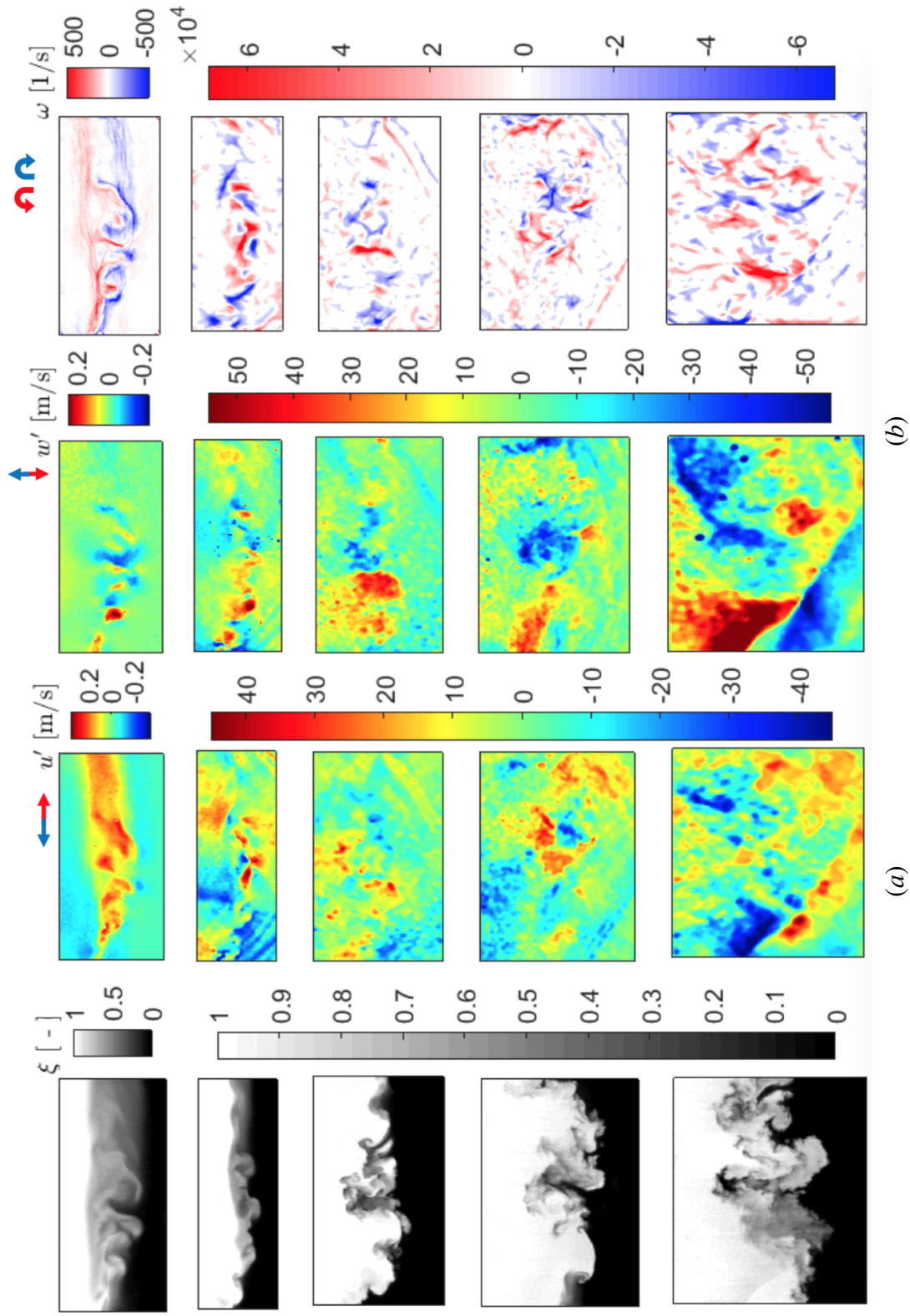
Figure 13: Representative field evolution results for the $M = 2.2$ case. From top to bottom: IC, PS1, PS2, PS3, PS4. From left to right: concentration ξ, global fluctuation transverse velocity $\hat{u}$, global fluctuation streamwise velocity $\hat{w}$, and vorticity ω.

This increased mixing at higher Mach number is explored further through probability density functions (PDFs) of concentration, as well as the density self-correlation across the mixing layer as discussed in Sec. 5.4.

The overall composition of the mixing layer (within $0.05 < \langle \xi \rangle < 0.95$) is obtained from two-dimensional PDFs of concentration by

$$\text{PDF}(\xi) = \int_{-0.5}^{0.5} \text{PDF}(\xi, \tilde{z}) \, d\tilde{z}, \qquad (5.1)$$

where $\tilde{z}$ is the vertical direction scaled by the 5-95% height of the interface. These PDFs are shown in Fig. 14 for the (a) $M = 1.6$ data and (b) $M = 2.2$ data. The PDFs show that a local peak near $\xi \sim 0.5$ reduces over time and appears to mix with the lighter ($\xi = 1$) fluid. This process occurs more rapidly in the $M = 2.2$ case and results in an increase in the contribution of $\xi > 0.5$ fluid at late time. This bias for mixing of the lighter fluid has been noticed elsewhere and is attributed to the greater inertia of the heavy fluid [44, 85]. Figures 14(a) and 14(b) also show a nearly monotonic increase of PDF(ξ) in time for $\xi = 0$ and $\xi = 1$ due to the development of spikes and bubbles in the mixing zone. A rapid increase in PDF(ξ) near $\xi = 1$ for the $M = 1.6$ case indicates that light gas is penetrating into the mixing layer without mixing, while the more gradual increase in PDF(ξ) near $\xi = 1$ for the $M = 2.2$ case shows that, while there is a larger fraction of light fluid in the mixing layer due to bubble development, this fluid is mixing with the surrounding gas as it penetrates the interface.

This same method of determining PDFs within the 5-95% mixing region is applied to the corresponding transverse and streamwise global velocity fluctuations as well. Global velocity fluctuations in the transverse direction (shown in Figs. 14(c) and 14(d) for the $M = 1.6$ and $M = 2.2$ cases, respectively) show a dual-peaked PDF($\hat{u}$) for the initial condition. The right peak seen in the inital condition PDFs is due to the positive velocity associated with the
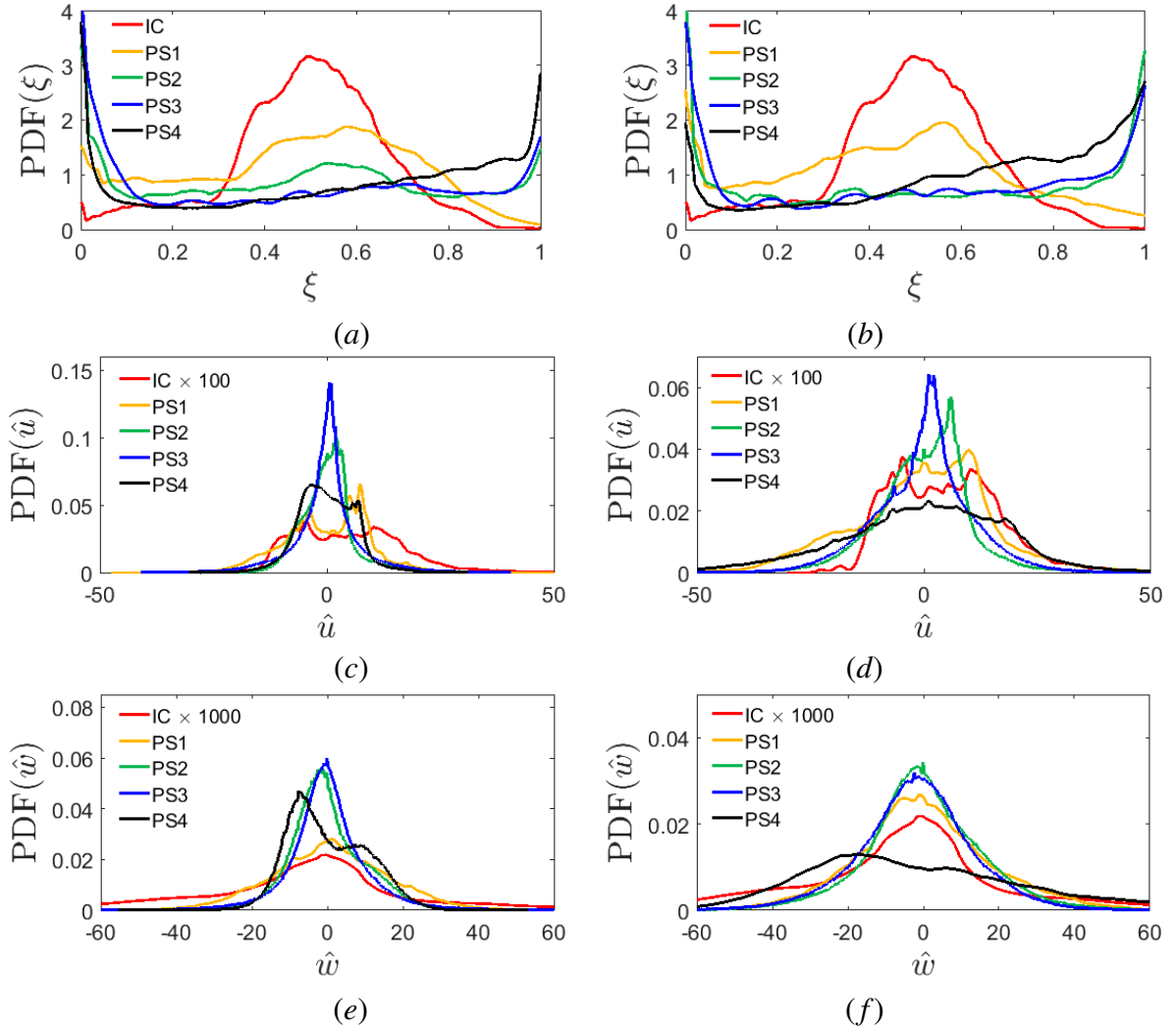
Figure 14: Probability density functions of (a) ξ for the $M = 1.6$ case, (b) ξ for the $M = 2.2$ case, (c) $\hat{u}$ for the $M = 1.6$ case, (d) $\hat{u}$ for the $M = 2.2$ case, (e) $\hat{w}$ for the $M = 1.6$ case, and (f) $\hat{w}$ for the $M = 2.2$ case. Units for $\hat{u}$ and $\hat{w}$ are m/s.

rightward-moving gas jet used to set up the shear layer, while the left peak corresponds to the distribution about the stationary $u = 0$ gas. This left peak is not centered on 0 m/s since it has been shifted away from zero by the subtraction of u_{avg} to obtain the $\hat{u}$ field. Following passage of the shock wave, the velocity increases by roughly two orders of magnitude and the two peaks begin moving closer together. This convergence of peaks continues through PS2, until they have combined into a single peak by PS3 for each case. By PS4, transverse velocity again begins to develop a dual-peaked structure, likely due to the outward-growth associated with expanding spikes and bubbles that have developed by this latest time.

In the streamwise direction, PDFs show (in Figs. 14(e) and 14(f) for the low and high Mach number cases, respectively) a nearly Gaussian distribution of velocity at the intial condition that increases by roughly three orders of magnitude following shock acceleration. The PDF distrubution peaks at PS3 for the $M = 1.6$ case and at PS2 for the $M = 2.2$ case, and this difference could be associated with an earlier transition to turbulence for the higher Mach number case. Further evidence of this transition occuring near PS3 for the $M = 1.6$ case and near PS2 for the $M = 2.2$ case is presented through measurements of density self-correlation and Reynolds number in Secs. 5.4 and 5.8, respectively. After reaching the peak value near $\hat{w} = 0$, the PDF($\hat{w}$) distribution takes on a dual-peaked structure due to the development of large-scale spikes and bubbles. This two-peaked structure of the PDFs for streamwise velocity begins sooner and shows greater spread in velocity by the latest time for the high Mach number case, though both cases show a larger peak associated with the upward-moving ($\hat{w} < 0$) spikes than for the downward-going ($\hat{w} > 0$) bubbles.

5.2 Spanwise-Averaged Profiles

Velocity and concentration profiles are investigated here, where the spanwise-averaged mole-fraction field is defined by

$$\langle \xi \rangle = \frac{1}{x_2 - x_1} \int_{x_1}^{x_2} \xi \, dx, \tag{5.2}$$

where x_1 and x_2 are the first and last column for which ξ measurements were obtained, respectively, such that the integral is performed across the entire width of the field for each experiment to yield a single profile. A similar approach was used for the transverse and streamwise global velocity fluctuations. These profiles from individual images are then scaled by h_{5-95}, and ensemble averaged to create a single profile at each time. Ensemble spanwise-averaged profiles for each post-shock time are shown in Fig. 15, with results for $M = 1.6$ experiments on the left, and profiles from the $M = 2.2$ case on the right.

The top row of Fig. 15 shows the spanwise-averaged concentration results. These profiles look very different from previously reported profiles [85] despite the similarities with these earlier studies. The difference comes from the chosen match-point for interface height scaling and ensemble averaging. Because each experiment produces interface of differing thickness, when scaling by the h_{5-95} and averaging results from individual runs, experiments must be matched at a chosen point. This match point will be the common location where profiles from each time will overlap, by definition. In previous experiments, the $\xi = 0.05$ (or $\xi = 0.95$) locations were used as match points, and profiles showed rough, irregular slopes matched at the corresponding $z/h_{5-95} = -0.5$ (or 0.5) locations. In the present work however, a more natural value of $\xi = 0.5$ was chosen as the match point. As a result, concentration results in Fig. 15 show more symmetric, "S"-shaped spanwise-averaged profiles which are centered on $z/h_{5-95} = 0$.
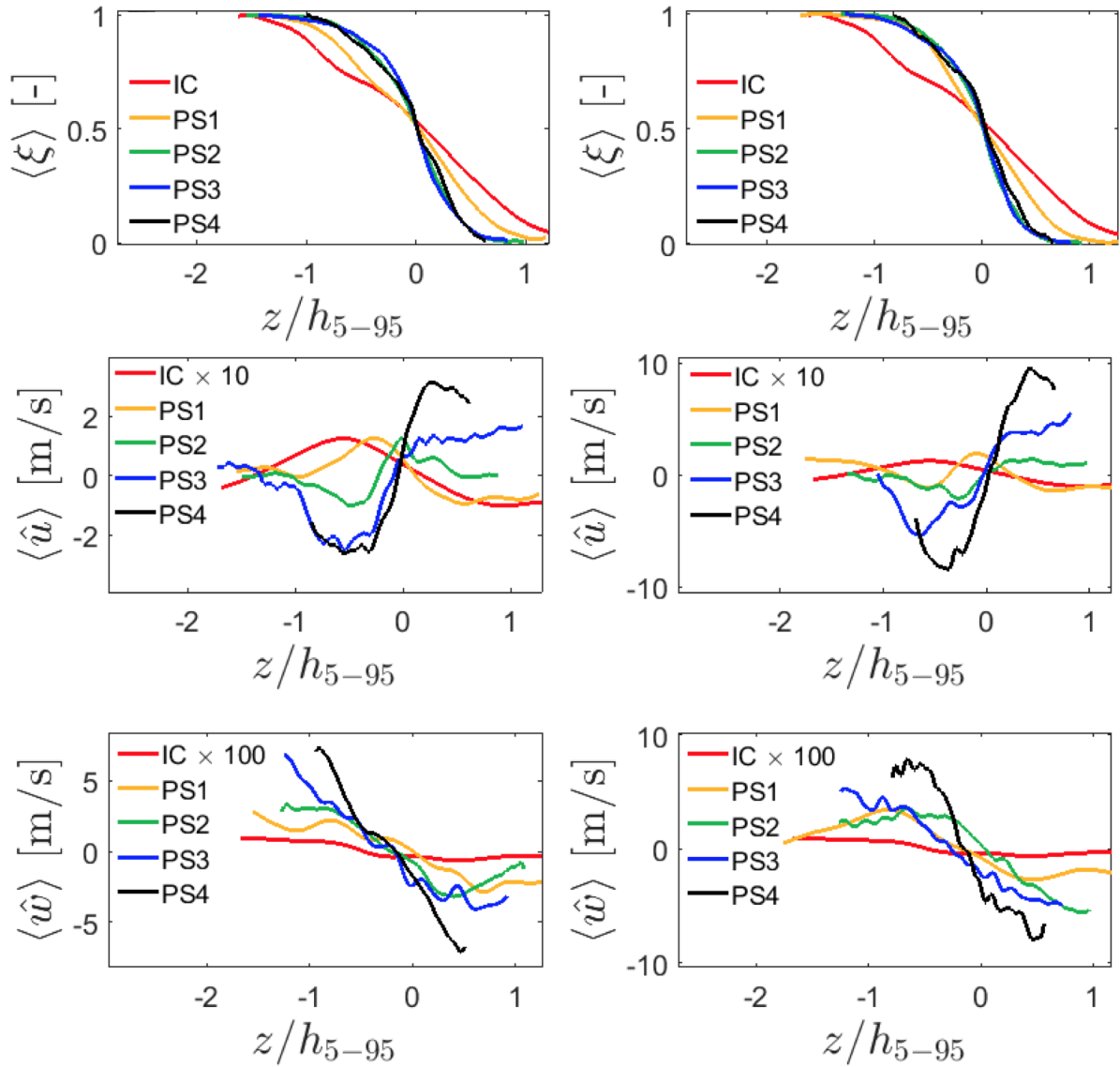
Figure 15: Spanwise-averaged profiles of concentration and velocity for M=1.6 (left) and M=2.2 (right). From top to bottom: Concentration, global transverse velocity fluctuations, and global streamwise velocity fluctuations.

The initial condition concentration profile shows a gradual slope with a kink in the profile just below the $z/h_{5-95} = -1$ location. This kink should be atributed to variability in the exact location of the shear-jet used in creating the initial condition interface, which is shown to be located at a similar z/h_{5-95} height in the transverse velocity profiles in the second row of Fig. 15. After shock, this gradual slope is shown to steepen in time, with a more rapid increase occuring for the higher Mach number case. This steepening in time is a result of pure ($\xi = 0$ or $\xi = 1$) gas being pushed into the mixing zone with the development of spikes and bubbles at late times. Consequently, bubbles will cause the $\langle \xi \rangle$ value to increase ever-closer to the interface midpoint above the $z/h_{5-95} = 0$ location, while spikes will drive the $\langle \xi \rangle$ value towards zero below the interface.

In the second row of Fig. 15, spanwise-averaged profiles are shown for the global transverse velocity fluctuations, $\hat{u}$. These profiles show the rightward-moving jet used to establish the shear layer intial condition occurring near $z/h_{5-95} = -0.7$, along with recirculation zones directly above and below the jet region. These features are also clear in the transverse velocity fields shown in Figs. 12 and 13. Following passage of the shock wave, global transverse velocity profiles for PS1 show compression and a nearly $10\times$ increase in jet velocity. The jet is also shown to push downwards from the top of the mixing layer towards the center of the mixing layer near $z/h_{5-95} = 0$. At higher M acceleration there is greater compression of the jet, which is also pushed deeper into the center of mixing layer when compared with the low M case. The velocity in the recirculation zone above the jet is accentuated as time progresses such that the entire region above the jet pushes leftward at late time. Alternatively, a monotonic increase in spanwise velocity with time is observed to occur below the interface, corresponding to bulk rightward motion below the interface midpoint. This increase in spanwise-averaged global transverse velocity above and below the interface is roughly $3\times$ greater for the higher Mach

number case than in the low Mach number experiments.

Finally, spanwise-averaged profiles of the global streamwise velocity fluctuations are shown in the bottom row of Fig. 15. While not easily seen in Fig. 15, the streamwise velocity in the initial condition is found to be positive above the interface and negative below it. This is due to the fact that the light gas is filled from the top of the tube and flows downward (with positive streamwise velocity), while the heavy gas is filled from the bottom of the tube and pushes upwards (with negative streamwise velocity) towards the interface. From the initial condition to PS1, velocities in the streamwise direction are shown to increase by more than two orders of magnitude. Each successive profile shows a general steepening in time, corresponding to an increase in velocity, with regions above the interface moving downwards with ever-increasing speed, and regions below the interface moving upwards increasingly rapidly. This trend is likely due to the development of the large-scale spikes and bubbles in the flow, where the light gas continues to push downwards through the interface, and the heavy gas approaches the mixing zone more readily with the development of penetrating spikes. Similar trends are observed for both the low and high Mach number cases, with slightly higher velocities by the latest time for the $M = 2.2$ case.

5.3   Mixing-layer Thickness

Threshold measurements of the $0.05 < \langle \xi \rangle < 0.95$ mixing-layer thickness, h_{5-95}, are made using a spanwise-averaged mole-fraction field similar to results discussed in the previous section, but with an important adjustment made to the interface. Since better collapse of the thickness measurements was obtained by removing large-scale structures from the mixing-layer, this interface adjustment is made prior to spanwise averaging the field. This is done by first finding

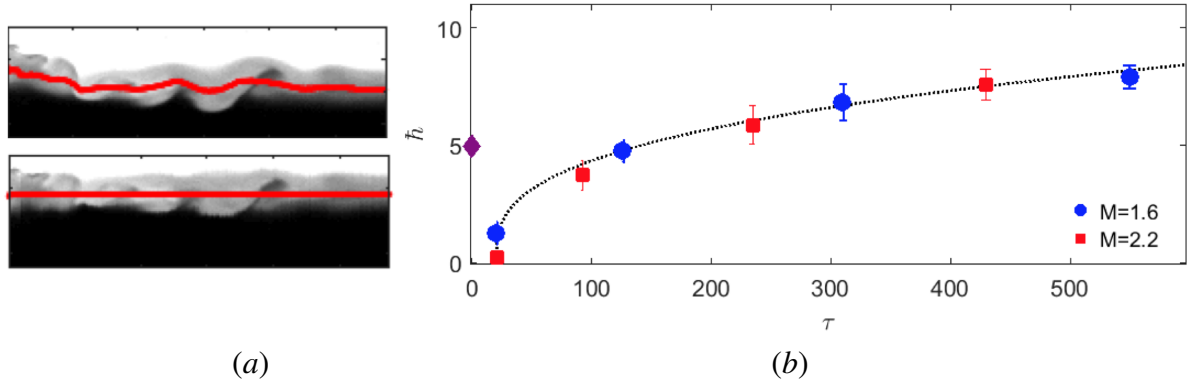(a)   (b)

Figure 16: Mixing layer thickness measurements. (a) Adjusted interface [bottom] eliminates additional height added by large-scale features present in the uncorrected mixing layer [top], and results in better collapse of thickness measurements. (b) Symbols show the average non-dimensional threshold measurements of the $0.05 < \langle \xi \rangle < 0.95$ region in time, error bars show the standard deviation from the 20 experiments, and dotted line shows a power-law fit to data.

the midpoint location between the $\langle \xi \rangle = 0.05$ and $\langle \xi \rangle = 0.95$ rows for each column, defined as z_0 and shown in Fig. 16(a) [top] as a red line across the mixing layer. Each column is then vertically shifted to bring all z_0 to the same height, as shown in Fig. 16(a) [bottom]. If the column was shifted upwards, the bottom of that column was padded with zeros, while if the column was moved downwards, the top of the column was filled with ones.

From the adjusted interface, threshold measurements of $h_{5-95\%}$ were obtained for each experiment and averaged to give a single thickness measurement at every post-shock time. Results were nondimensionalized using h_0^* – the pre-shock interface thickness scaled by the compressed value $(1 - V_0/W_i)$ – and the dominant wavenumber,

$$\hbar = (h_{5-95\%} - h_0^*)k_0, \tag{5.3}$$

and time was nondimensionalized as,

$$\tau = tV_0A^+h_0^*k_0^2, \tag{5.4}$$

where t is the time, V_0 is the post-shock interface velocity, A^+ is the post-shock Atwood

number, and k_0 is the dominant wavenumber. The value for k_0 is determined from the initial conditions as $k_0 = 2\pi/\lambda_0$, similarly to [79]. These nondimensional thickness measurements are shown in Fig. 16(b), where error bars show the standard deviation at each time, and the dotted line shows a power-law fit to data such that

$$(h_{5-95\%} - h_0^*)k_0 = a(tV_0A^+h_0^*k_0^2)^\theta,$$ (5.5)

where a is unity and the power law fits $\theta = 0.34 \pm 0.01$. This value of θ is similar to previously reported values ($0.25 \leq \theta \leq 0.5$) in the work of Dimonte [25, 26], Prasad [60], Weber [85], and Jacobs [38].

A similar measure of the mixing layer thickness, called the mixing product thickness, h_p, can be obtained from the adjusted spanwise-averaged profiles. This has been used previously by Cook [20] and Weber [85], and is defined as

$$h_p = \int_{-\infty}^{\infty} \xi_p(\langle \xi \rangle)\,dz,$$ (5.6)

where

$$\xi_p(\xi) = \begin{cases} 2\xi & \text{for } \xi \leq 0.5 \\ 2(1 - \xi) & \text{for } \xi > 0.5 \end{cases}$$ (5.7)

is the mixture composition, and an equimolar mixture is $\xi_p = 1$. This quantity is shown in Fig. 17 and these integral measurements of thickness are found to be linearly proportional to the threshold measurement h_{5-95} value ($h_p = 0.57h_{5-95}$). This proportionality is identical to measurements made by Weber [85], despite the different growth exponent θ due to the adjustment used to remove large-scale features from the interface.

The threshold and integral measurements of the mixing layer thickness explored above do not differentiate between mixed gas and gas that is penetrating the interface but remains
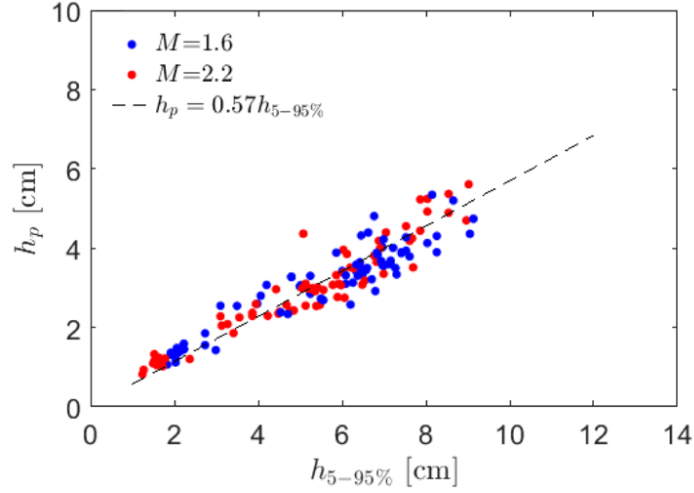
Figure 17: Comparison of mixing layer thickness definitions showing that integral measurements are proportional to threshold measurements of thickness.

unmixed. For this, a definition of "mixedness" will need to be defined. The relative amount of molecular mixing occuring within the interface can be characterized as a ratio of a mixing length to an entrainment length. Multiple definitions have been proposed, but perhaps the two most commonly referenced global mixing parameters are those by Youngs [90]:

$$\Theta = \frac{\int_{-\infty}^{\infty} \langle \xi(1-\xi) \rangle dz}{\int_{-\infty}^{\infty} \langle \xi \rangle \langle 1-\xi \rangle dz},$$ (5.8)

and a similar definition by Cook & Dimotakis [20]:

$$\Xi = \frac{\int_{-\infty}^{\infty} \langle \xi_p \rangle dz}{h_p}.$$ (5.9)

For both cases, a ratio with a value of 1 corresponds to a fully homogenized fluid without interpenetrating perturbations, while a value of 0 indicates no molecular mixing of the fluids. Both definitions were compared in [19] and [47] and were shown to give very similar results. This similarity between the two definitions of global mixing is also seen in the current studies. The latter definition was used by Weber [85], and produced results comparable to those found for Ξ in the present work.
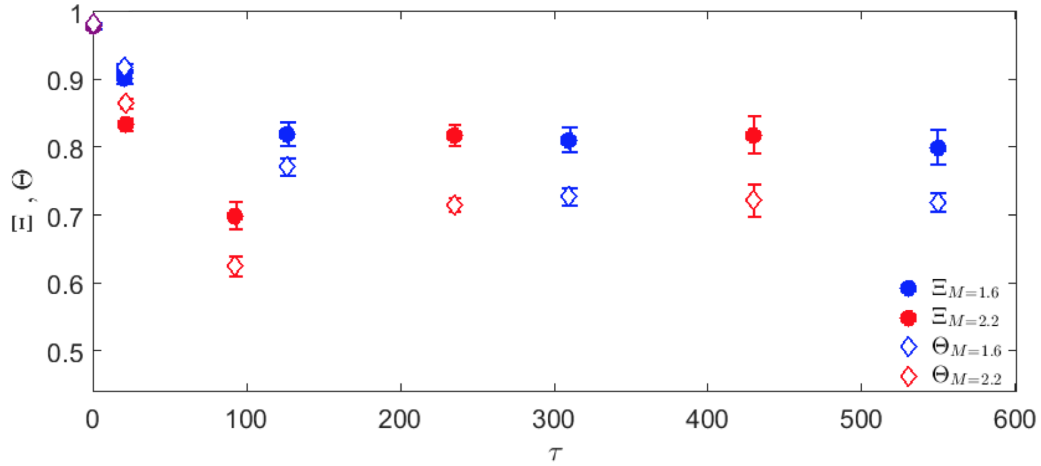
Figure 18: Comparison of mixing definitions Ξ and Θ for the low and high Mach number experiments.

As shown in Fig. 18, the value of both Θ and Ξ is found to strictly decrease in time for the low M case, and decrease before increasing again for the high M case. Youngs' definition of mixedness is larger than Cook's definition during compression, while the opposite is true at late times. This is a similar trend to what has been previously reported, where Θ underpredicts the initial homogenization of fluid and then also underpredicts the ensuing fluid mixing at later times when compared to Ξ values of mixedness. Measurements of Ξ show that both Mach numbers reach a final value near 0.8, which is the asymptotic value reported after the onset of turbulent mixing in Rayleigh-Taylor simulations [19], while Θ approaches a value slightly below 0.8. Simulations have also shown that the cross from Θ over-predicting to under-predicting the mixed fluid measurement occurs following the rapid growth of Θ and Ξ that occurs after reaching the minimum value. This could be used to argue that, like the $M = 2.2$ case, the $M = 1.6$ value for Θ and Ξ could also decrease between PS1 and PS2 before increasing again at later times; however, this effect is not captured at the times the interface was studied in this work. Future work should aim to better resolve the time between PS1 and

PS2 (especially for the low Mach number case) to investigate if such a trend is observed.

5.4   Density Self-correlation

The density self correlation (DSC) is another measure of fluid mixing, where a value of zero indicates perfectly mixed fluid. Density self-correlation is an important quantity for turbulence modeling and appears in the production term of the mass flux equation. DSC is involved in the conversion of potential energy into kinetic energy, and is defined by

$$b = -\langle \rho' \left(\frac{1}{\rho}\right)' \rangle ,$$ (5.10)

where brackets denote spanwise averaging and primes indicate fluctuations. The DSC is determined by first calculating the density field from the measured concentration field and the known post-shock density values

$$\rho = \rho_2^\dagger + (\rho_1^\ddagger - \rho_2^\dagger)\xi ,$$ (5.11)

where a single dagger indicates once-shocked gas, a double dagger represents twice-shocked gas (by the incident and reflected shock wave), and ρ_1 and ρ_2 are the density of the light and heavy gas, respectively. The fluctuating component of the density field and $1/\rho$ is then determined using the spectral filtering method described in Sec. 4.4.

The mean value of DSC as a function of height through the mixing layer is shown in Fig. 19(a) for the $M = 1.6$ case and in Fig. 19(b) for the $M = 2.2$ case. Results were obtained similarly to spanwise-averaged profiles, where individual DSC profiles were calculated and scaled by the h_{5-95} height. Ensemble averaging the 20 DSC measurements from individual experiments allowed for a mean value at every post-shock time at each Mach number to be obtained. This averaging technique is shown in Fig. 19(c), where the colored lines show
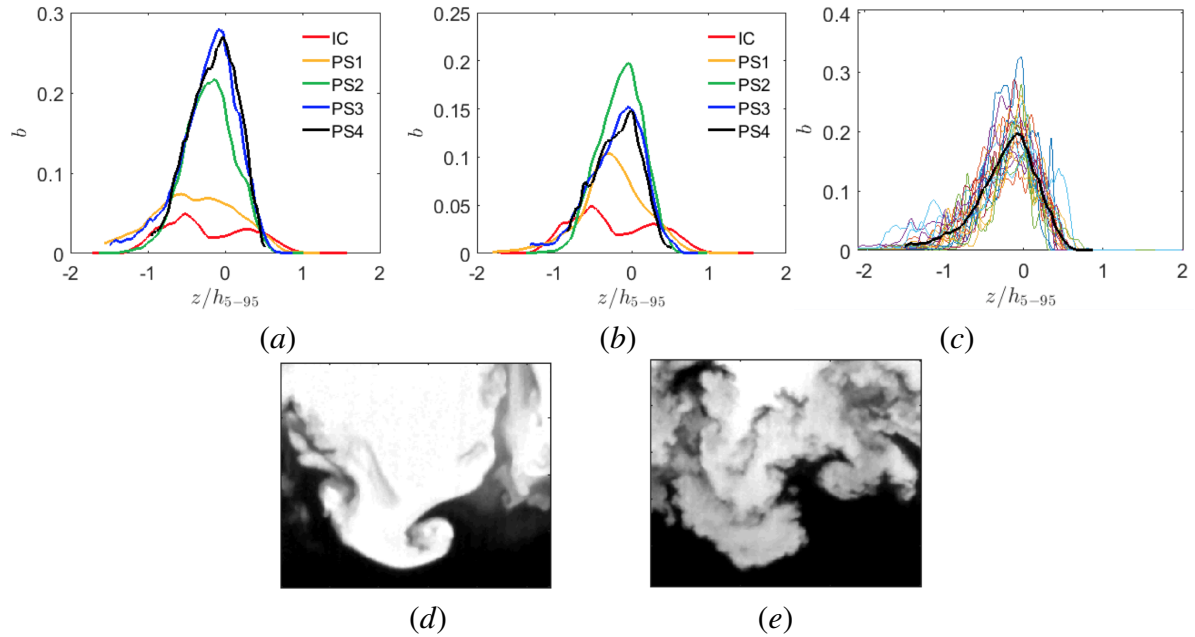
Figure 19: Average density self-correlation measurements for the (a) $M = 1.6$ case, and (b) $M = 2.2$ case. Example of ensamble averaging over 20 experiments to obtain mean b measurements shown in (c), where colored lines show data from individual experiments and the black line shows the campaign average. Details of the ξ field showing evidence of mixing differences at the latest post-shock time for the (d) low Mach number, and (e) high Mach number cases.

density self-correlation measurements for individual experiments, while the thick black line shows the average DSC profile for that post-shock time.

Measurements of the DSC through the mixing layer for the low Mach number case show general growth in time, indicating that the fluid is less mixed at later times. This is likely the result of large spikes and bubbles carrying unmixed fluid into the mixing layer. However, for the high Mach number case, DSC measurements show growth through PS2, before decaying at PS3 and PS4. The turn-around in the DSC trend for the $M = 2.2$ case is caused by the increased mixing and breakdown to smaller scales associated with a transition to turbulence. This difference in the behavior of the DSC between the low and high Mach number cases can

be better understood by a comparison of the ξ (and ultimately ρ) fields at the latest post-shock time. Figure 19(d) shows a bubble and spike that has developed at PS4 for the $M = 1.6$ case, showing the largely unmixed fluid penetrating the mixing layer leading to an increase in DSC. Conversely, Fig. 19(e) shows a similar feature for the $M = 2.2$ case, where the spike and bubble have smaller-scale features and increased mixing (more gray regions within the mixing layer) relative to the low Mach number case, leading to a reduction of the DSC mixing measurement at late times. This evidence of transition to turbulence occuring by PS2 for the $M = 2.2$ case is further supported by Reynolds number measurements discussed in Sec. 5.8.

5.5 Scalar Dissipation Rate

In order to make sense of the spatial properties of mixing structures and the rate at which mixing is occuring within the mixing layer, the dissipation rate (χ) is explored in this section. The dissipation rate is an important factor governing mixing and is defined by

$$\chi = \mathscr{D}\nabla\xi \cdot \nabla\xi,$$ (5.12)

where the diffusion coefficient $\mathscr{D} = 1.5 \times 10^{-5}$ m^2/s for the gas pair used in the current studies. This dissipation rate is calculated for every experiment, and representative results for χ at each post-shock time are shown overlaid on the corresponding concentration field in Fig. 20.

The dissipation rate fields from the first post-shock time for both Mach numbers show long features that stretch horizontally across the image. Larger values for χ are found at the bottom boundary of the mixing layer when compared with values at the top boundary, and a greater dissipation rate appears to occur on the left side of the interface, near the horizontal gas injection site used to create the shear layer initial condition. These horizontally-oriented
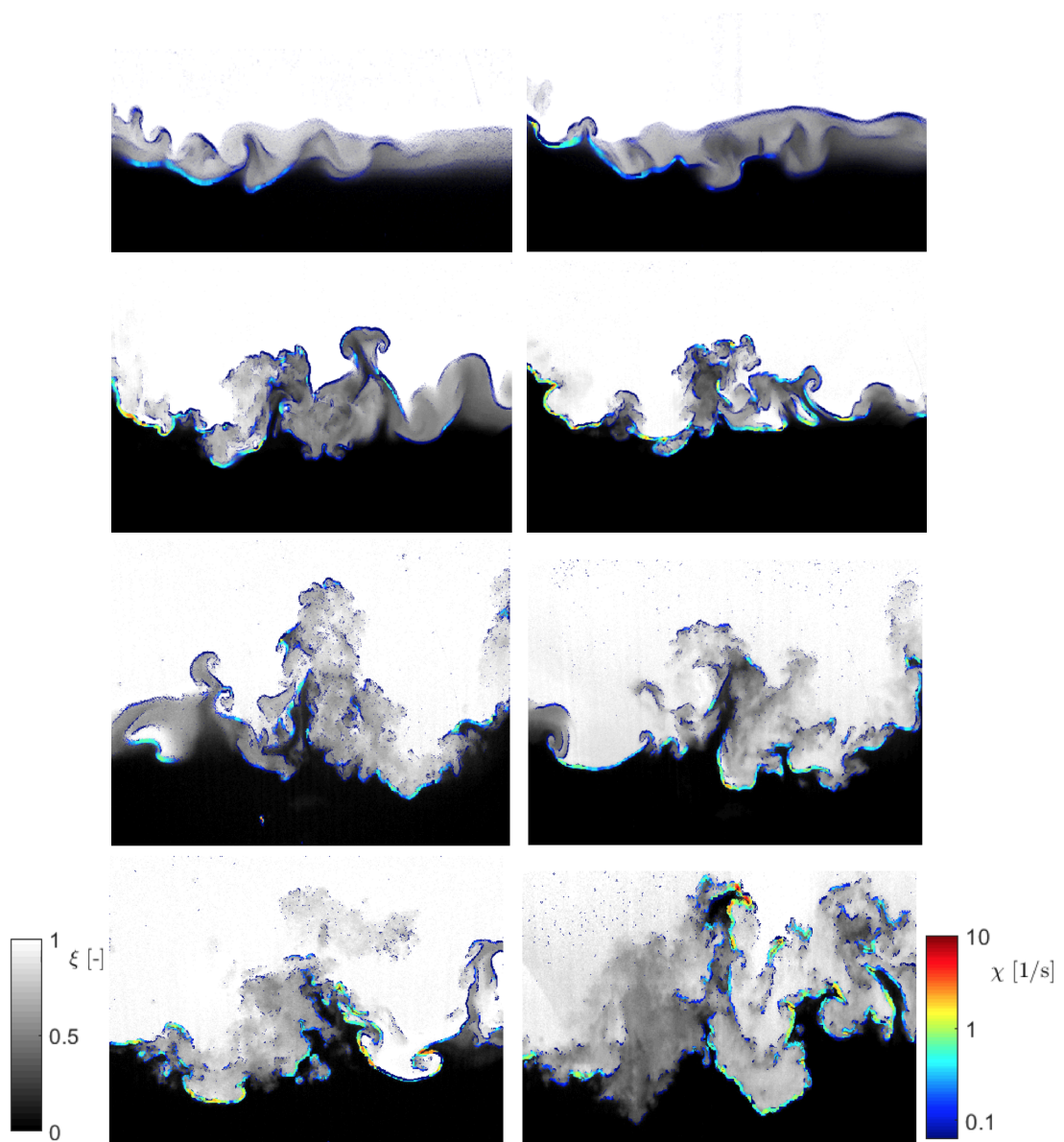
Figure 20: Representative dissipation fields, χ, overlaid on the mole fraction field, ξ. From top to bottom: PS1, PS2, PS3, PS4. Left column is $M = 1.6$, right column is $M = 2.2$.
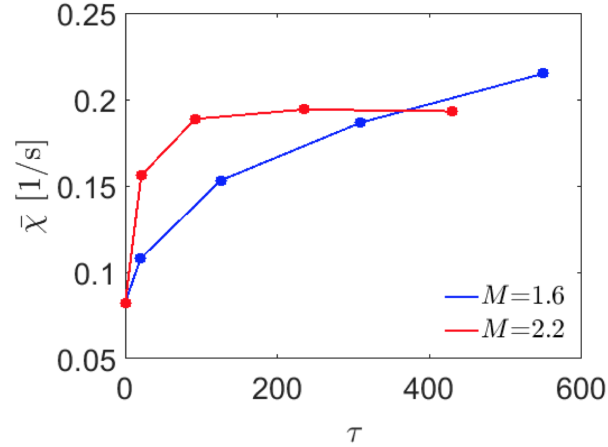
Figure 21: Average dissipation rate ($\overline{\chi}$) in time for the low (blue) and high (red) Mach number cases.

features seen at PS1 begin to gain some vertical height in sucessive post-shock times as spike and bubble features begin to appear and the mixing layer starts its growth. By the latest times, the dissipation structures do not appear to have an obvious preferred direction, and appear somewhat chaotic with a large curvature. It should also be noted that the greater dissipation rate originally occuring on the left side of the interface at early times is not preserved at later times, when the largest χ values are found scattered throughout the mixing layer.

The mean dissipation rate in the $0.05 < \langle \xi \rangle < 0.95$ region ($\overline{\chi}$) is reported as a function of time in Fig. 21, with the time nondimensionalized using Eq. 5.4. The mean dissipation rate increases rapidly at early post-shock times (with a more rapid increase for the higher Mach number case) before the growth slows at later times. This growth continues through all post-shock times for the low M case, while $M = 2.2$ results show growth through PS3, before a slight decay in average dissipation rate for PS4. This trend in $\overline{\chi}$ makes physical sense when other metrics of the mixing layer are considered. Since large, unmixed spikes and bubbles are known to penetrate the mixing layer at late times in the $M = 1.6$ experiments, this brings pure
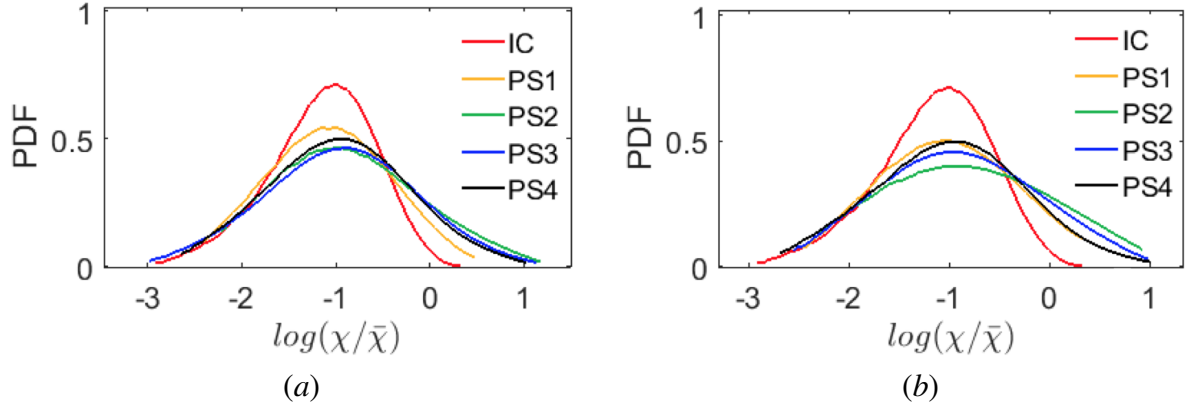
Figure 22: PDFs of the dissipation rate for the initial condition and four post-shock times for the (a) $M = 1.6$ case and (b) $M = 2.2$ case.

light gas in contact with pure heavy gas, where a larger dissipation rate is expected. However, for the higher Mach number case, this interpenetration of gas is shown to be accompanied by a breakdown to smaller scales and mixing. This mixing that occurs between the pure light and pure heavy gases ultimately slows the rate a which dissipation occurs, leading to the decrease in $\bar{\chi}$ seen at PS4 for the $M = 2.2$ case. Results shown in Fig. 21 follow a trend similar to results from Weber [79], although the $\bar{\chi}$ values found in the present work are smaller at later times and do not show as large a decay between latest times for the $M = 2.2$ case.

PDFs of the $\log_{10}$ of dissipation rate scaled by its mean value are shown in Fig. 22. While the left side of the PDFs show good agreement between all times, the right side of the PDFs (corresponding to larger dissipation rates), shows that there is both greater spread and larger values of the dissipation rate occuring after shock acceleration within the mixing layer. For the low Mach number case, a larger portion of the mixing layer contains a greater dissipation rate at each successive time as the right leg of the PDF pushes rightward in time. For this low M case, the last three PS times show very good agreement, while the right leg of this PDF begins to move inward at the latest time for the higher M case. This move toward smaller

dissipation rates at PS4 agrees well with the drop in $\overline{\chi}$ seen at the latest times seen in Fig. 21 for the $M = 2.2$ case.

5.6 Energy Spectra

The scale-dependence of concentration and velocity fluctuations is reported here using one-dimensional energy spectra. This approach has been applied previously for variable density turbulence in the Rayleigh-Taylor instability [21, 86, 62, 55, 9], as well as shocked gas-curtain experiments [78, 77] and shear layer interface experiments [85], which have reported the existence of a $k^{-5/3}$ inertial range. These experiments showing a $k^{-5/3}$ scaling in the inertial range are corroborated by simulations [51, 36, 70], while other simulations found $k^{-3/2}$ to fit better at late times [74], and others still found turbulence spectra that did not scale well with either $k^{-5/3}$ or $k^{-3/2}$ [14, 34]. Zhou [91] has suggested that the spectrum of RMI turbulence should scale as $k^{-3/2}$ in the inertial range before reducing to the classical Kolmogorov $k^{-5/3}$ scaling at late times.

One-dimensional scalar variance energy spectra, $E_{\xi}(k_x)$, are computed in the self-similar (horizontal) direction within the region $0.05 < \langle \xi \rangle < 0.95$, and results are averaged over rows from all 20 experiments at each post-shock time. To reduce the influence of camera noise and extend the spectrum at the highest wavenumbers, an interlacing technique is used [40, 85] where the Fourier coefficient, $F(\xi(x))$, is multiplied by the complex conjugate of the Fourier coefficient of the adjacent row,

$$E_{\xi}(k_x) \approx F(\xi_j(x))F^*(\xi_{j+1}(x)). \qquad (5.13)$$

This averaged, interlaced scalar variance energy spectrum is shown in Figs. 23(a) and 23(b) for the low and high Mach number case, respectively. All spectra have been normalized by
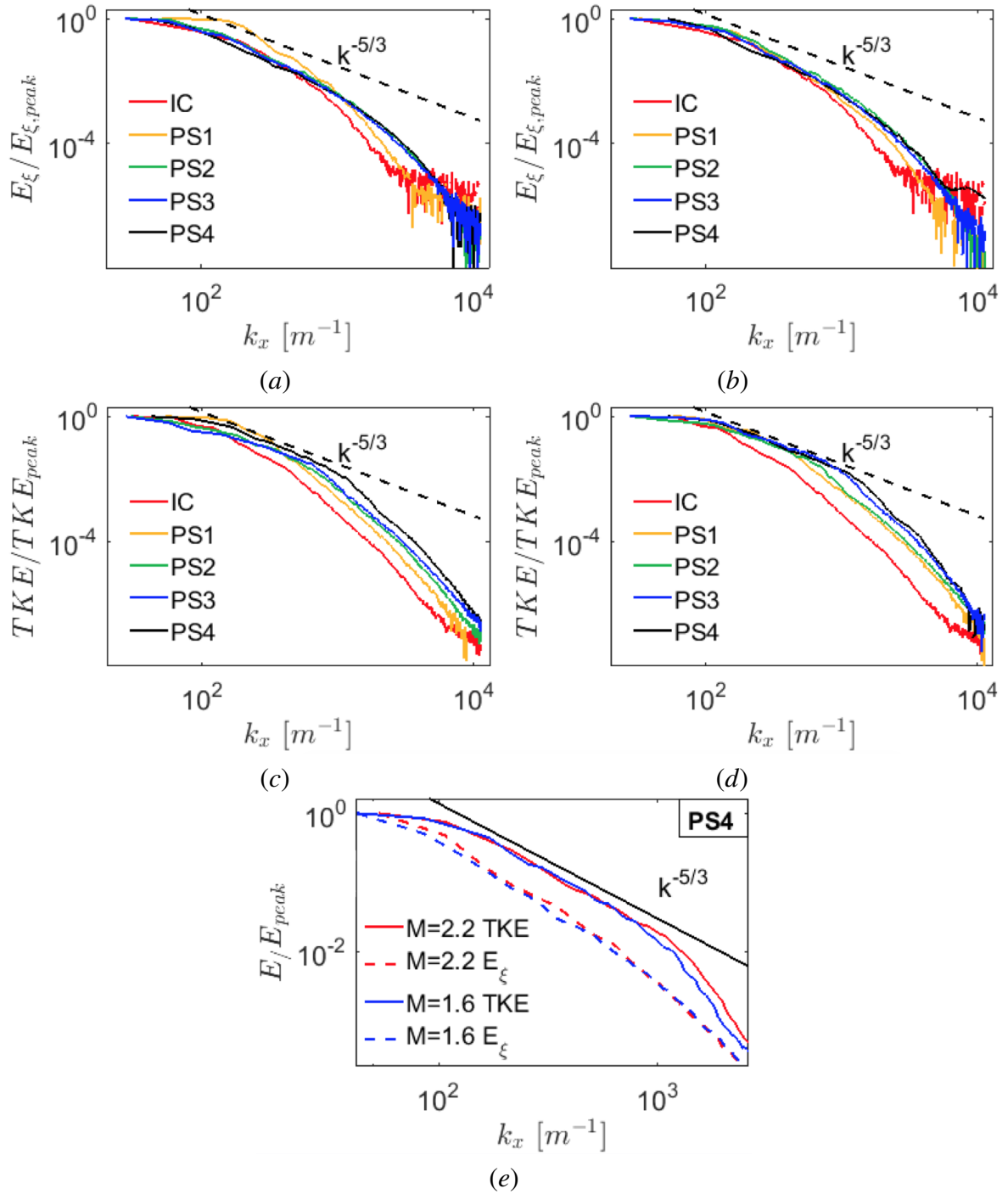
Figure 23: Comparison of spectra showing evolution of relative energy. (a) Scalar variance energy spectra for $M = 1.6$ case, (b) Scalar variance energy spectra for $M = 2.2$ case, (c) TKE spectra for $M = 1.6$ case, (d) TKE spectra for $M = 2.2$ case, and (e) comparison of spectra at latest time.

their peak value for a better comparison of relative energy distribution in time. While spectra appear to tend toward a $k^{-5/3}$ inertial range by the latest time for both Mach numbers, this slope is only achieved at the lowest wavenumbers near $k_x \simeq 100$ before dropping off at higher wavenumbers. Comparison of Figs. 23(a) and 23(b) show that, for the high Mach number case, spectra approach their late-time form slightly more quickly than for the low Mach number case.

A similar approach was taken to obtain the turbulent kinetic energy (TKE) spectra. Since only two components of velocity were measured, we will refer to these spectra as planar TKE. Because these flows are variable density, it is required to consider both density and velocity when calculating TKE. As with the scalar variance energy spectra, the planar TKE spectrum is calculated using the interlacing method,

$$TKE(k_x) \approx F(\mathcal{K}_j(x))F^*(\mathcal{K}_{j+1}(x)), \tag{5.14}$$

where $\mathcal{K}$ is the density-weighted planar turbulent kinetic energy defined using the global velocity fluctuations,

$$\mathcal{K} = \frac{\rho}{2}[\hat{u}^2 + \hat{w}^2]. \tag{5.15}$$

These energy spectra have also been normalized by their peak value, and results are shown in Figs. 23(c) and 23(d) for the low and high Mach number case, respectively. Planar TKE spectra show the clear development of a $k^{-5/3}$ inertial range which spans over roughly a decade of wavenumber space. We also note a monotonic increase in relative energy at small scales in time, with a more rapid increase occuring for the $M = 2.2$ experiments. Comparison of the spectra at the latest time is shown in Fig. 23(e), and late-time planar TKE spectra show slightly higher energy at larger wavenumbers, whereas scalar variance spectra show good agreement for both the low and high Mach number cases.
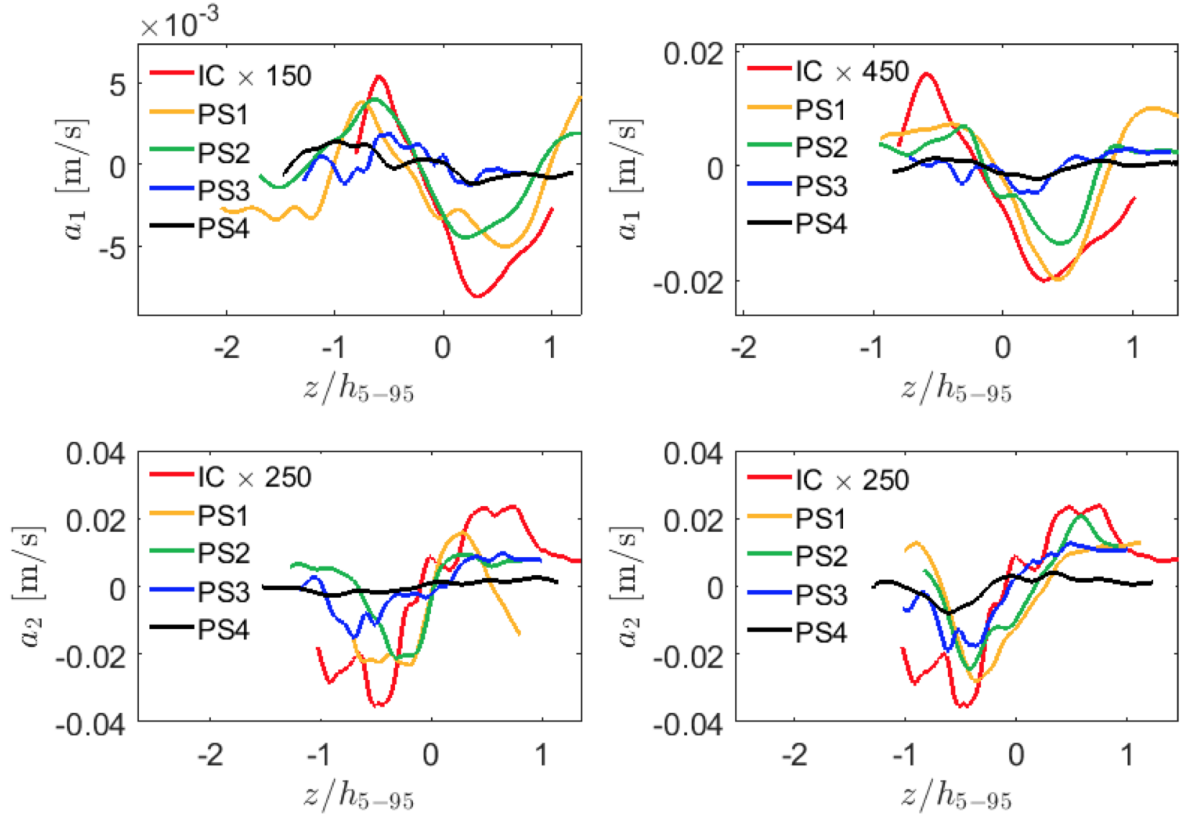
Figure 24: Directional turbulent mass-flux velocity measurements across the mixing layer for each post-shock time. Left column is $M = 1.6$ case, while right is $M = 2.2$. Top row is turbulent mass-flux velocity in the transverse direction, and bottom row is in the streamwise direction.

5.7 Reynolds Stresses

Turbulent mass-flux velocity (TMFV) is a primary turbulent source term for mixing, and it appears as a prefactor in the production term for the turbulent kinetic energy evolution equation. Here the density-weighted TMFV is studied, which is defined as

$$a_i = \frac{\langle \rho' u_i' \rangle}{\langle \rho \rangle}, \tag{5.16}$$

where the brackets denote spanwise averaging, primes indicate fluctuations determined using the spectral method in Sec. 4.4, the index i denotes the direction (such that for the streamwise

TMFV the w' field is used, while u' is used to calculate the transverse TMFV), and Eq. (5.11) was used to calculate density from the measured concentration fields. Figure 24 shows how directional TMFV varies across the height of the interface for the initial condition and at each post-shock time for the low and high Mach number cases. Here, a subscript of 1 corresponds to the transverse direction (x) while a subscript of 2 corresponds to the streamwise direction (z). We see from Fig. 24 that transverse turbulent mass-flux velocity is generally positive above the interface midpoint and becomes negative below the interface midpoint, while the streamwise turbulent mass-flux velocity is generally negative above the interface and positive below it. The spanwise-averaged streamwise TMF velocity shows that turbulent mass flux is upward at the top of the mixing zone and downward below it, indicating that the mixing zone is growing; however, the values of TMF velocity decay in time, indicating that this growth should be slowing down as time progresses. This "slowing growth" of the interface is consistent with the interface thickness measurements of Sec. 5.3. Outside of the turbulent mixing zone, the TMF velocities tend towards zero both above and below the interface in each direction. We also note slightly larger values of turbulent mass-flux velocity in both directions for the high Mach number case, indicating greater production of turbulent kinetic energy due to the larger velocities imparted by the stronger shock.

Turbulent mass-flux velocity measurements can also be used in calculating Reynolds stresses in the flow. Reynolds stresses are the mean forces per unit area imposed on the mean flow by the turbulent fluctuations, and they are defined by

$$R_{ij} = \langle \rho u_i'' u_j'' \rangle = \langle \rho \rangle \langle u_i' u_j' \rangle - \langle \rho \rangle a_i a_j + \langle \rho' u_i' u_j' \rangle, \tag{5.17}$$

where double primes denote Favre-averaged velocity fluctuations. The present work will explore each of the three terms on the right hand side of Eq. (5.17) individually, as well as the
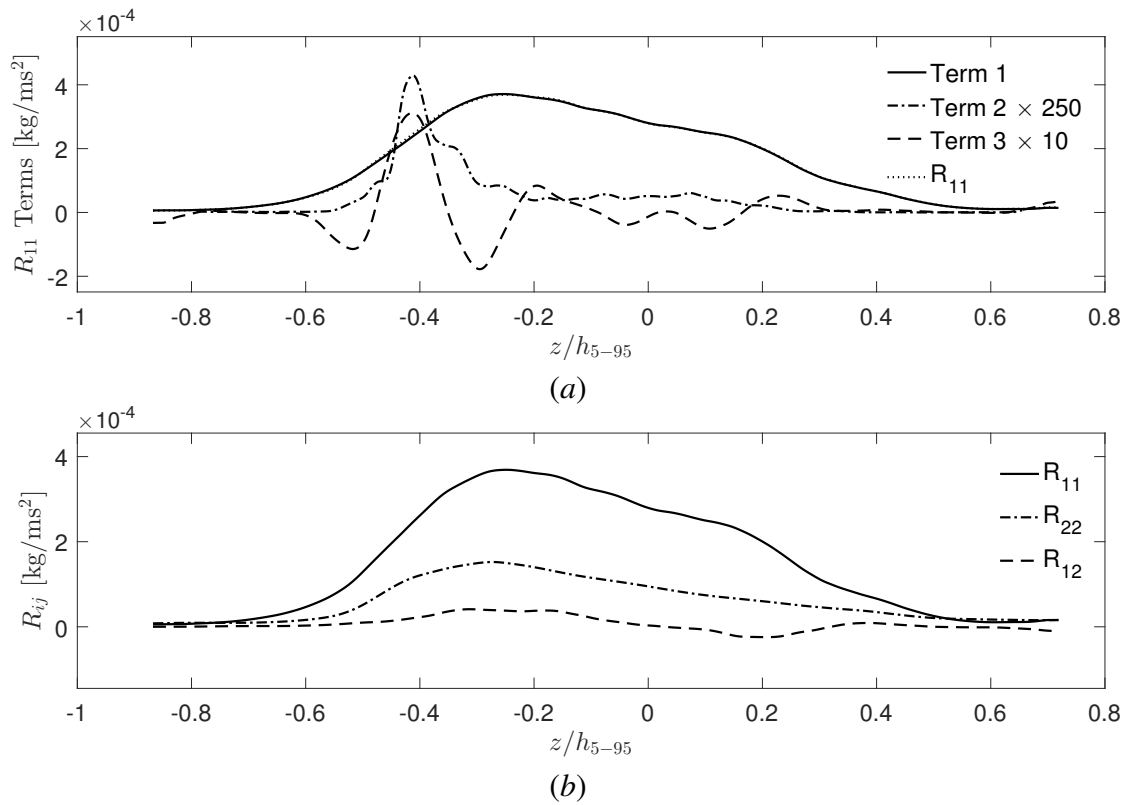
Figure 25: Reynolds stress measurements at the initial condition. (a) Comparison of terms in equation 5.17 for the transverse component of Reynolds stress. (b) The three measured components of the Reynolds stress across the mixing layer.

three (of six) components of Reynolds stress that have been obtained directly through simultaneous measurements of concentration and velocity. Representative results for each of the three terms on the right-hand side of the streamwise Reynolds stress component in equation 5.17 are shown individually for the initial condition in figure 25(a). Term 1 is the mean density-velocity correlation, and is clearly the dominant term. Term 2 is the the mass flux term and is roughly $250 \times$ smaller than term 1. Term 3 is the triple correlation term, which is shown to be roughly an order of magnitude smaller than the mean density-velocity correlation term. A similar trend in the importance of term 1 over the other two terms has been seen previously by [5] and [31]. The effect of the shear jet used in creating the initial condition is clearly visible in the mass flux and triple correlation terms, where the large velocity fluctuations within the jet region dominate the stresses near the $z/h_{5-95} = -0.4$ height.

In addition to viewing individual terms of the Reynolds stress components, the value of the components themselves can be compared as a function of position across the turbulent mixing zone; this is shown for the initial condition in figure 25(b). A comparison of the three measured components of the Reynolds stress tensor shows that the transverse and streamwise components remain positive throughout the mixing zone, and each shows a tendency toward zero value away from the interface, indicating the greatest forces from turbulent fluctuations are occurring near the center of the mixing zone. The transverse component (R_{11}) is shown to dominate at the initial condition due to the horizontal motion of the shear layer interface. Finally, the cross term remains near zero throughout much of the mixing layer, with generally negative values in the lower portion of the layer and generally positive values in the top portion. It should be noted that these direct measurements can also be used to help constrain and validate turbulence models.
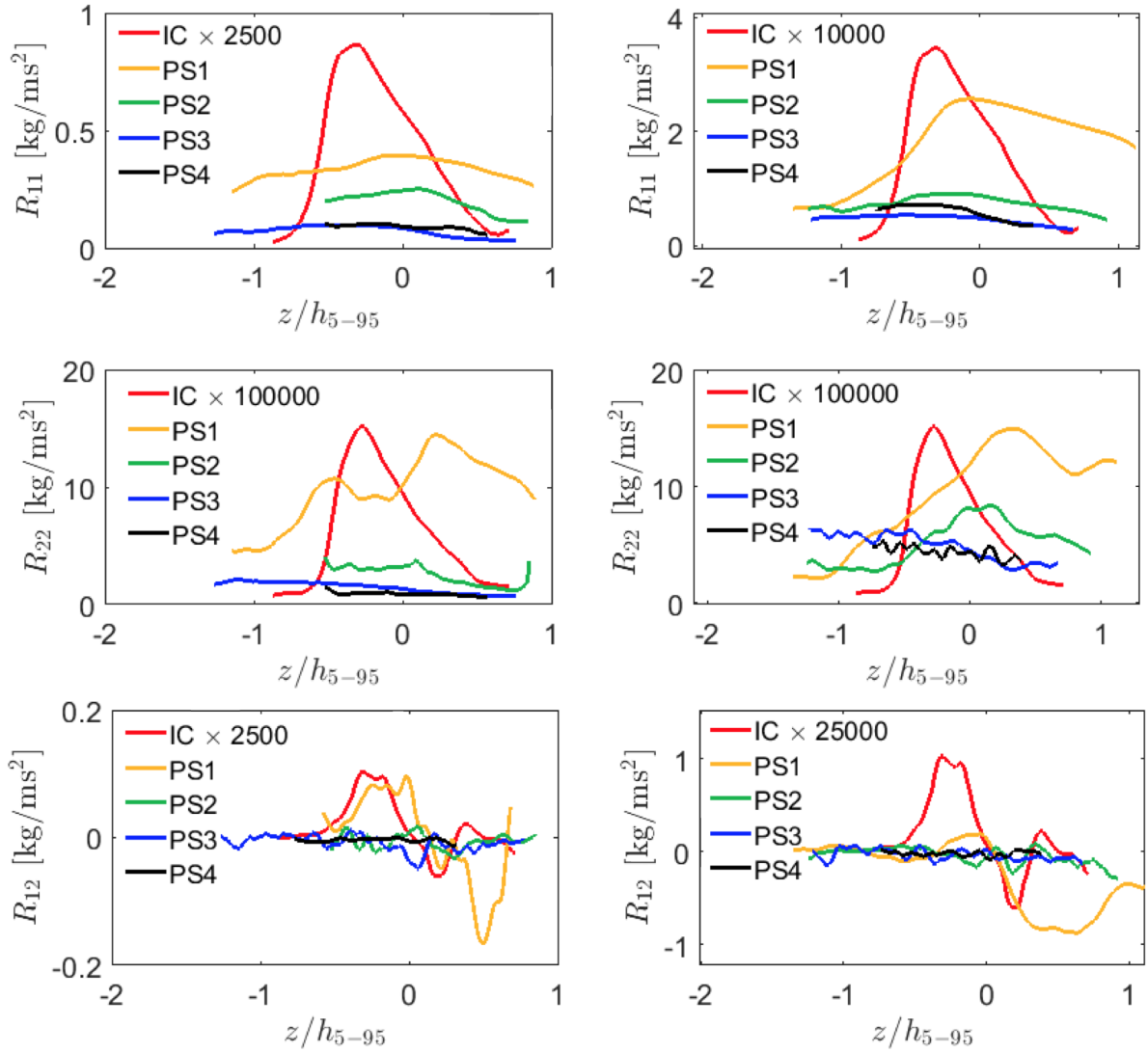
Figure 26: The three measured components of the Reynolds stress across the mixing layer for the $M = 1.6$ case (left) and the $M = 2.2$ case (right). From top to bottom: transverse stresses, streamwise stresses, cross-term stresses.

The evolution of each component of the Reynolds stresses is shown in Fig. 26. A comparison of the three measured components of the Reynolds stress tensor shows that, following passage of the shock wave, the streamwise component (R_{22}) is dominant. At early times the interface exhibits a tendency towards zero value away from the mixing zone, indicating the greatest forces from turbulent fluctuations are occurring near the center of the mixing zone. However, as time progresses, a decay in Reynolds stress is seen at the center of the mixing layer, while stresses near the top of the layer begin to grow. This same trend is seen for the transverse Reynolds stresses. This bias for growth in Re_{ii} at the top of the mixing layer is likely related to the increase seen in PDFs of ξ near $\xi = 1$, which is attributed to the greater inertia of the heavy fluid. In other words, more mixing is occuring near the top of the mixing layer, and with this mixing come increased Reynolds stresses. Finally, the cross term decays toward zero throughout much of the mixing layer, with generally positive values in the top portion of the layer and generally negative values in the lower portion.

5.8   Reynolds Number

The Reynolds number is a ratio of inertial forces to viscous forces, and can be calculated by dividing the product of a characteristic length scale and flow velocity by the kinematic viscosity of the flow. For the Taylor Reynolds number, the characteristic length scale is chosen to be the Taylor microscale such that

$$Re_\lambda = \frac{u_{rms}\lambda_T}{\nu} , \tag{5.18}$$

where $u_{rms} = \sqrt{\langle u'^2 \rangle}$ is the root-mean-square velocity using local velocity fluctuations in the self-similar (transverse) direction, λ_T is the Taylor microscale, and ν is the kinematic viscosity.
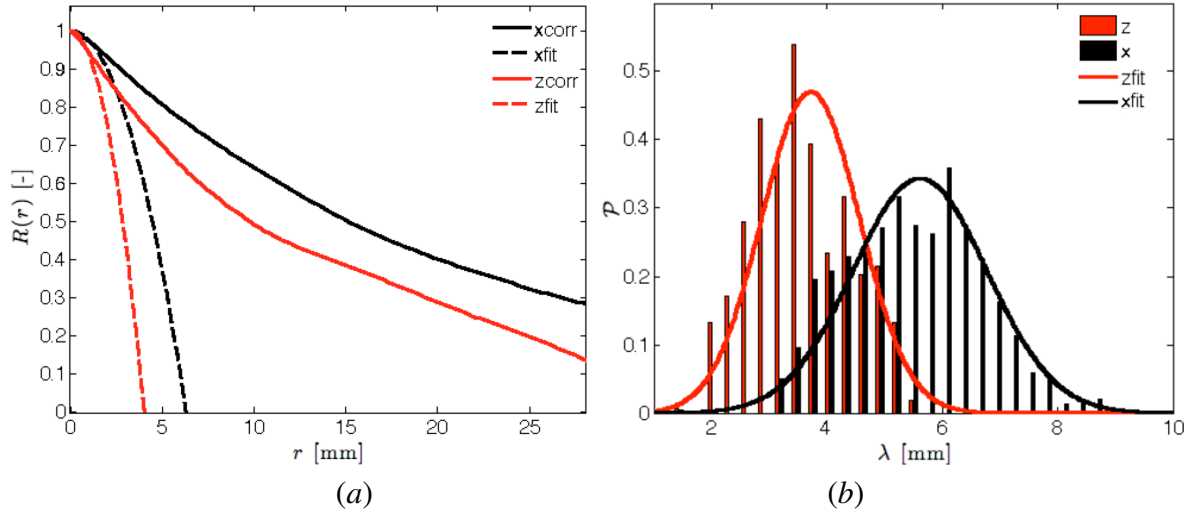
Figure 27: Representative measurements using each of the two methods employed to calculate the Taylor microscale. Results shown for (a) the autocorrelation method, where λ_T is determined by the r-intercept of the osculating parabola fit to the autocorrelation curve, and (b) the variance method, where the peak of the distribution fit defines λ_T.

To understand the time evolution of the Taylor Reynolds number in the current experiments, we will first look closer into determining the values λ_T and ν.

The Taylor microscale is the length scale at which viscosity will begin to significantly affect the flow, and it is found here using two methods. In the first, the Taylor microscale is defined based on the curvature of the velocity autocorrelation. The velocity autocorrelation,

$$R(r) = \frac{\langle \hat{u}(x)\,\hat{u}(x+r)\rangle}{\langle(\hat{u})^2\rangle} \, , \tag{5.19}$$

is an even function, and is therefore symmetric such that $R(-r) = R(r)$. As such, the first terms in the Taylor series are

$$R(r) = 1 + \frac{1}{2}\frac{d^2 R(0)}{dr^2}r^2 \tag{5.20}$$

$$= 1 - \frac{r^2}{\lambda_T^2} \, . \tag{5.21}$$

As done by many others [13, 62, 58, 85], the Taylor microscale can then be calculated directly

from the curvature of the autocorrelation,

$$\lambda_T = \left[-\frac{1}{2} \frac{d^2 R(0)}{dr^2} \right]^{-1/2} . \tag{5.22}$$

The osculating parabola is fit using the central seven points of the autocorrelation; that is the central $r = 0$ point, the adjacent three points, and the corresponding three points on the $-r$ side of the correlation. This is performed for both the streamwise and transverse velocity, such that directional $\lambda_{T,i}$ are found, and a nominal Taylor microscale is calculated by $\lambda_T = \sqrt{\lambda_{T,x}^2 + \lambda_{T,z}^2}$. The directional Taylor microscales using this method are shown in Fig. 27(a), where the autocorrelations are the solid lines, the osculating parabolas are the dashed lines, and the directional Taylor microscales are determined by the r-intercepts of the dashed lines.

Equivalently, the Taylor microscale can be calculated from the variance and the first-derivative,

$$\lambda_{T,x} = \left[\frac{2 \left\langle (\hat{u})^2 \right\rangle}{\left\langle \left(\frac{\partial \hat{u}}{\partial x} \right)^2 \right\rangle} \right]^{1/2} , \quad \lambda_{T,z} = \left[\frac{2 \left\langle (\hat{w})^2 \right\rangle}{\left\langle \left(\frac{\partial \hat{w}}{\partial z} \right)^2 \right\rangle} \right]^{1/2} . \tag{5.23}$$

This method is shown in Fig. 27(b), where the peak of the distribution fit defines the directional Taylor microscale. Again, this is calculated in each direction and a single value for the Taylor microscale is determined from the square root of the sum of the squares. Results using the autocorrelation method and the variance method are then averaged to give a representative λ_T measurement at the initial condition and at each post-shock time; the evolution of this representative λ_T is shown in nondimensional time for the two Mach numbers in Fig. 28.

The representative Taylor scale is shown to be roughly 7 mm for the initial condition shear-layer flow. Following shock acceleration of the interface, the Taylor scale is shown to decrease rapidly for both Mach number cases. This decrease continues to give a value $\lambda_T \simeq 2.6$ mm at PS2 for both cases, though this decrease in λ_T occurs slightly faster for the higher M case.
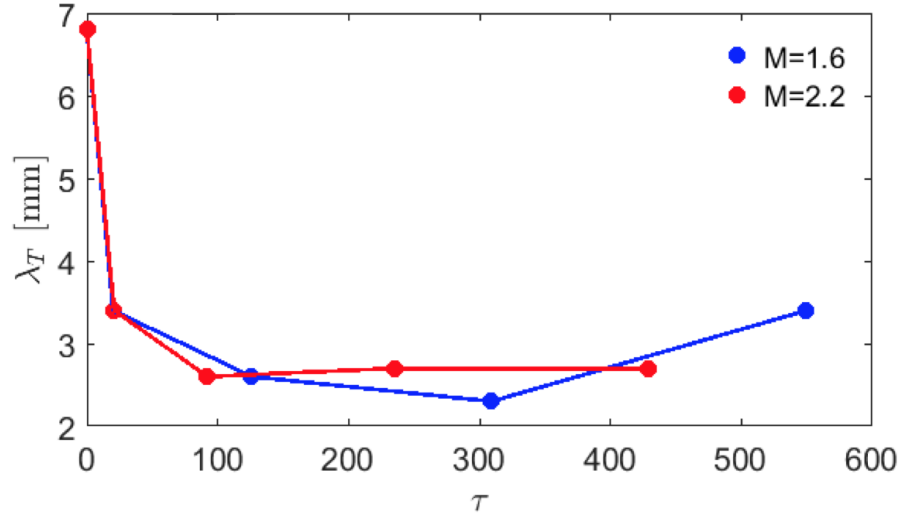
Figure 28: Taylor scale measurements as a function of time for the low and high Mach number cases.

While the $M = 2.2$ experiments show an increase in the Taylor microscale following PS2, low M results indicate a continued decrease in λ_T through PS3 before increasing only at the latest post-shock time. By PS4, the low M Taylor microscale has reached a value just above 3 mm, while the λ_T determined from the high M experiments lies just below 3 mm. It should be noted that this method of determining λ_T was also carried out using the scalar field data (similarly to [85]), and results using velocity yielded λ_T measurements about 50% those founding using ξ-field measurements.

The final value needed to determine the Taylor Reynolds number is the kinematic viscosity, ν. The kinematic viscosity is computed as $\nu(\xi) = \mu_{\mathrm{mix}}/(\rho_2^\dagger + (\rho_1^\ddagger - \rho_2^\dagger)\xi)$ and the dynamic viscosity is averaged from the viscosities of each species, weighted by its mole fraction and molecular weight [67, 85],

$$\mu_{\mathrm{mix}} = \frac{\sum_i \mu_i \xi_i \sqrt{MW_i}}{\sum_i \xi_i \sqrt{MW_i}}. \tag{5.24}$$

Since the average mole fraction within the mixing layer is $\xi \sim 0.5$, $\nu(\xi)$ is evaluated at this
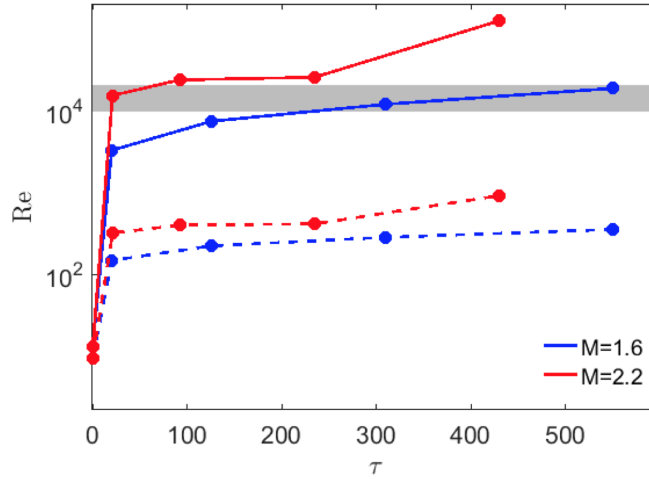
Figure 29: Taylor Reynolds number (dashed) and outer-scale Reynolds number (solid) as a function of time. The gray band indicates the threshold for turbulent mixing [28].

value, giving 1.6×10^{-5} m^2/s.

With values determined for each term in the Taylor Reynolds number equation, Re_λ can now be determined at each time in the development of the instability using Eq. (5.18). The Taylor Reynolds number is shown in Fig. 29 for the low and high Mach number cases as the dotted blue and red lines, respectively. Results show a rapid increase in Re_λ following passage of the shock wave, with a larger increase in Reynolds number for the high Mach number case. With Re_λ determined for each post-shock time, an estimate of the outer-scale Reynolds number can also be found using the relation $Re = (3/20)Re_\lambda^2$, which holds for isotropic turbulence [59]. Outer-scale Reynolds number results are shown also in Fig. 29 as solid lines. By showing the turbulent transition zone shaded in gray [28], we note that the flow just barely passes through this zone by PS4 for the low Mach number case; however, the flow is passed this transition zone by PS2 for the high Mach number case. This is consistent with earlier findings in this report indicating a transition to turbulence occuring near PS2 for the $M = 2.2$ case, such as DSC profile measurements and streamwise global velocity fluctuation distributions.

Chapter 6

Conclusions

Simultaneous PIV and PLIF experiments were conducted in the Wisconsin Shock Tube Laboratory to obtain concurrent, full-field concentration and velocity field measurements of a shock-accelerated shear layer interface. PLIF images were corrected to account for the nonuniform laser profile, laser sheet divergence, and Beer's law attenuation to show mole fraction, while PIV particle image pairs gave corresponding velocity fields. Velocity fields were matched to concentration results using a field-matching technique requiring the use of target images obtained with each camera prior to every experiment. Once the post-shock fields had been matched to the same coordinate system, a spectral method was used to decompose the flow into mean and fluctuating components.

The RMI mixing layer measurements obtained in this study allowed, for the first time in this regime, calculations of turbulence quantities giving insight into the development of turbulence in a shock-accelerated mixing layer. Results showed evidence of power-law growth of the mixing layer, as $\hbar \propto \tau^{0.34}$ after adjusting the interface to remove height added from large scale features. A comparison of mixing layer thickness definitions has shown that integral measurements are proportional to threshold measurements of thickness. Evidence of a transition to turbulence occuring by the latest time for the low Mach number case, but as early as PS2 for the high Mach number case was first seen by calculating the density self-correlation across the mixing layer.

Transverse velocity fields show the break-up of the rightward-going jet used to establish the initial condition shear layer, while streamwise velocity fields show the amplification of alternating upward and downward-traveling gas, which develops into spike and bubble structures at late times. We find that turbulent mass-flux velocities show very different behavior depending on the direction considered, and vary greatly depending on position across the turbulent mixing zone. TMF velocities were also shown to be larger in magnitude by the latest time when accelerated by a stronger shock, indicating a greater production of turbulent kinetic energy, as well as a tendency towards zero value outside of the mixing layer. Reynolds stress calculations showed that the mean density-velocity correlation term is of greatest importance when determining the mean forces per unit area imposed on the mean flow by the turbulent fluctuations, which is in agreement with results from previous work. The streamwise component of the Reynolds stress was shown to be dominant and have the largest values in the center of the mixing zone.

Spanwise-averaged profiles of the concentration field were matched at the $\xi = 0.5$ level and showed a steepening in time, likely due to the penetration of pure light-gas bubbles and heavy argon spikes. Profiles of the global transverse velocity fluctuations showed the compression of the rightward-going jet used to create the IC interface, with greater compression occuring for the high M case, while profiles of the global streamwise velocity fluctuations showed ever-increasing downward velocity above the interface and upward velocity below the interface. This is consistent with gas below the interface pushing upward through the interface with the development of spikes, and gas above the interface moving downward as bubbles form at late times.

Planar TKE spectra included density effects and showed a tendency toward a $k^{-5/3}$ slope in the inertial range (covering a much larger region of wavenumber space than seen for the scalar

variance energy spectra), and a more rapid movement toward this final state for the higher Mach number case. A monotonic increase in relative energy was seen at the small scales, and acceleration by a stronger shock has also been shown to increase the relative amount of energy transferred to the small scales by the latest times. The Taylor microscale was calculated using two methods, and was used to determine the Taylor Reynolds number for the flow. Outer-scale Reynolds numbers were obtained from Taylor Reynolds numbers at each time in the development of the instability, and provided further evidence of a transition to turbulence occuring by PS4 for the low Mach number experiments, and by as early as PS2 for the high Mach number case.

Bibliography

[1] M. H. Anderson, B. P. Puranik, J. G. Oakley, P. W. Brooks, and R. Bonazza, *Shock tube investigation of hydrodynamic issues related to inertial confinement fusion*, Shock Waves **10** (2000), 377–387.

[2] D. Arnett, *The role of mixing in astrophysics*, Astrophys J. Suppl. Ser. **127** (2000), no. 2, 213–217.

[3] X. S. Asay-Davis, P. S. Marcus, M. H. Wong, and I. dePater, *Jupiter's shrinking great red spot and steady oval ba: Velocity measurements with the 'advection corrected correlation image velocimetry' automated cloud-tracking method*, Icarus **203** (2009), 164–188.

[4] R. Aure and J. W. Jacobs, *Particle image velocimetry study of the shock-induced single mode richtmyer–meshkov instability*, Shock Waves **18** (2008), 161–167.

[5] B. J. Balakumar, G. C. Orlicz, J. R. Ristorcelli, S. Balasubramanian, K. P. Prestridge, and C. D. Tomkins, *Turbulent mixing in a richtmyer–meshkov fluid layer after reshock: velocity and density statistics*, J. Fluid Mech. **696** (2012), 67–93.

[6] B. J. Balakumar, G. C. Orlicz, C. D. Tomkins, and K. P. Prestridge, *Simultaneous particle-image velocimetry–planar laser-induced fluorescence measurements of richtmyer-meshkov instability growth in a gas curtain with and without reshock*, Physics of Fluids **20:124103** (2008).

[7] S. Balasubramanian, G. C. Orlicz, K. P. Prestridge, and B. J. Balakumar, *Experimental*

study of initial condition dependence on richtmyer-meshkov instability in the presence of reshock, Physics of Fluids **24** (2012), 034103.

[8] G. J. Ball and R. A. East, *Shock and blast attenuation by aqueous foam barriers: influence of barrier geometry*, Shock Waves **9** (1999), 37–47.

[9] A. Banerjee, W. N. Kraft, and M. J. Andrews, *Detailed measurements of a statistically steady Rayleigh—Taylor mixing layer from small to high atwood numbers*, J. Fluid Mech. **659** (2010), 127–190.

[10] R. Bonazza and B. Sturtevant, *X-ray measurements of growth rates at a gas interface accelerated by shock waves*, Phys. Fluids **8** (1996), no. 9, 2496–2512.

[11] M. Brouillette and B. Sturtevant, *Experiments on the Richtmyer-Meshkov instability: Small-scale perturbations on a plane interface*, Phys. Fluids A **5** (1993), no. 4, 916—930.

[12] G. L Brown and A. Roshko, *On density effects and large structure in turbulent mixing layers*, J. Fluid Mech. **64** (1974), no. 04, 775–816.

[13] F. H. Champagne, V. G. Harris, and S. Corrsin, *Experiments on nearly homogeneous turbulent shear flow*, J. Fluid Mech. **41** (1970), no. 01, 81.

[14] R. H. Cohen, W. P. Dannevik, A. M. Dimits, D. E. Eliason, A. A. Mirin, Y. Zhou, D. H. Porter, and Paul R. Woodward, *Three-dimensional simulation of a Richtmyer—Meshkov instability with a two-scale initial perturbation*, Phys. Fluids **14** (2002), no. 10, 3692.

[15] B. D. Collins and J. W. Jacobs, *Plif flow visualization and measurements of the*

richtmyer–meshkov instability of an air/sf6 interface, J. Fluid Mech. **464** (2002), 113–136.

[16] B. D. Collins and J. W. Jacobs, *PLIF flow visualization and measurements of the Richtmyer–Meshkov instability of an air/SF6 interface*, J. Fluid Mech. **464** (2002), 113–136.

[17] T. J. B. Collins, A. Poludnenko, A. Cunningham, and A. Frank, *Shock propagation in deuterium-tritium-saturated foam*, Phys. Plasmas **12** (2005), no. 062705.

[18] A. W. Cook, *Artificial fluid properties for large-eddy simulation of compressible turbulent mixing*, Physics of Fluids **19:055103** (2007).

[19] A. W. Cook, W. Cabot, and P. L. Miller, *The mixing transition in Rayleigh–Taylor instability*, J. Fluid Mech. **511** (2004), 333–362.

[20] A. W. Cook and P. E. Dimotakis, *Transition stages of Rayleigh–Taylor instability between miscible fluids*, J. Fluid Mech. **443** (2001), 69–99.

[21] S. B. Dalziel, P. F. Linden, and D. L. Youngs, *Self-similarity and internal structure of turbulence induced by Rayleigh—Taylor instability*, J. Fluid Mech. **399** (1999), 1–48.

[22] B. A. Davy and D. T. Blackstock, *Measurements of the refraction and diffraction of a short n wave by a gas-filled soap bubble*, J. Acoust. Soc. Am. **49** (1971), no. 3, 732–737.

[23] C. F. Delale, S. Nas, and G. Tryggvason, *Direct numerical simulations of shock propagation in bubbly liquids*, Physics of Fluids **17** (2005), no. 121705.

[24] M. Delius, F. Ueberle, and W. Eisenmenger, *Extracorporeal shock waves act by shock wave-gas bubble interaction*, Ultrasound in Med. and Biol. **24** (1998), no. 7, 1055–1059.

[25] G. Dimonte and M. Schneider, *Turbulent Richtmyer-Meshkov instability experiments with strong radiatively driven shocks*, Phys. Plasmas **4** (1997), no. 12, 4347–4357.

[26] ———, *Density ratio dependence of Rayleigh–Taylor mixing for sustained and impulsive acceleration histories*, Phys. Fluids **12** (2000), 304.

[27] P. E. Dimotakis, *The mixing transition in turbulent flows*, J. Fluid Mech. **409** (2000), 69–98.

[28] P. E. Dimotakis, *The mixing transition in turbulent flows*, J. Fluid Mech. **409** (2000), 69–98.

[29] W. Eisenmenger, *The mechanisms of stone fragmentation in eswl*, Ultrasound in Med. and Biol. **27** (2001), no. 5, 683–693.

[30] A. Abakumov et al., *Studies of film effects on the turbulent mixing zone evolution in shock tube experiments*, Proceedings of the fifth international workshop on compressible turbulent mixing (1996).

[31] S. Gerashchenko and K. P. Prestridge, *Density and velocity statistics in variable density turbulent mixing*, Journal of Turbulence **16** (2015), 1011–1035.

[32] S. M. Gracewski, G. Dahake, Z. Ding, S. J. Burns, and E. C. Bach, *Internal stress wave measurements in solid subjected to lithotripter pulses*, J. Acoust. Soc. Am. **94** (1993), 652–661.

[33] F. F. Grinstein, *Coarse grained simulation and turbulent mixing*, Cambridge: Cambridge University Press, 2016.

[34] F. F. Grinstein, A. A. Gowardhan, and A. J. Wachtor, *Simulations of Richtmyer—Meshkov instabilities in planar shock-tube experiments*, Phys. Fluids **23** (2011), no. 3, 034106.

[35] D. M. Heim, D. Jesch, and J. B. Ghandhi, *Size-scaling effect on the velocity field of an internal combustion engine, part ii: Turbulence characteristics*, International Journal of Engine Research **15** (2014), no. 2, 193–208.

[36] D. J. Hill, C. Pantano, and D. I. Pullin, *Large-eddy simulation and multiscale modelling of a Richtmyer—Meshkov instability with reshock*, J. Fluid Mech. **557** (2006), 29–61.

[37] J. W. Jacobs and V. V. Krivets, *Experiments on the late-time development of single-mode richtmyer–meshkov instability*, Physics of Fluids (2005).

[38] J. W. Jacobs, V. V. Krivets, V. Tsiklashvili, and O. A. Likhachev, *Experiments on the Richtmyer–Meshkov instability with an imposed, random initial perturbation*, Shock Waves **23** (2013), no. 4, 407–413.

[39] M. A. Jones and J. W. Jacobs, *A membraneless experiment for the study of richtmyer–meshkov instability of a shock- accelerated gas interface*, Physics of Fluids **9** (1997), 3078–3085.

[40] S. A. Kaiser and J. H. Frank, *Imaging of dissipative structures in the near field of a turbulent non-premixed jet flame*, P. Combust. Inst. **31** (2007), no. 1, 1515–1523.

[41] L. Houas L and I. Chemouni, *Experimental investigation of richtmyer–meshkov instability in shock tube*, Physics of Fluids (1996).

[42] D. Oron G. Erez L. Levin D. Shvarts L. Erez, O. Sadot and G. Ben-Dor, *Study of the membrane effect on turbulent mixing measurements in shock tubes*, Shock Waves **10** (2000), 241–251.

[43] E. Leinov, G. Malamud, Y. Elbaz, L. A Levin, G. Ben-Dor, D. Shvarts, and O. Sadot, *Experimental and numerical investigation of the Richtmyer-Meshkov instability under re-shock conditions*, J. Fluid Mech. **626** (2009), 449–475.

[44] D. Livescu and J. R. Ristorcelli, *Variable-density mixing in buoyancy-driven turbulence*, J. Fluid Mech. **605** (2008), 145–180.

[45] F. E. Marble, E. E. Zukoski, J. W. Jacobs, G. J. Hendricks, and I. A. Waitz, *Shock enhancement and control of hypersonic mixing and combustion*, 26th AIAA, SAE, ASME, and ASEE, Joint Propulsion Conference, Orlando, FL, July 16-18 (1990).

[46] J. McFarland, D. Reilly, S. Creel, C. McDonald, T. Finn, and D. Ranjan, *Experimental investigation of inclined interface richtmyer-meshkov instability before and after reshock*, Experiments in Fluids **55** (2014).

[47] J. P. Mellado, S. Sarkar, and Y. Zhou, *Large–eddy simulation of rayleigh–taylor turbulence with compressible miscible fluids*, Physics of Fluids **17** (2005).

[48] E. E. Meshkov, *Instability of a shock wave accelerated interface between two gases*, NASA Technical Translation **13** (1970), 1–14.

[49] E. E. Meshkov, *Instability of the interface of two gases accelerated by a shock wave*, Fluid Dyn **4** (1972), 101–104.

[50] K. Mikaelian, *Turbulent mixing generated by Rayleigh–Taylor and Richtmyer-Meshkov instabilities*, Physica D **36** (1989), 343–357.

[51] A. R. Miles, B. Blue, M. J. Edwards, J. A. Greenough, J. F. Hansen, H. F. Robey, R. P. Drake, C. Kuranz, and D. R. Leibrandt, *Transition to turbulence and effect of initial conditions on three-dimensional compressible mixing in planar blast-wave-driven systems*, Phys. Plasmas **12** (2005), no. 5, 056317.

[52] R. V. Morgan, R. Aure, J. D. Stockero, J. Greenough, W. Cabot, O. A. Likhachev, and J. W. Jacobs, *On the late-time growth of the two-dimensional richtmyer–meshkov instability in shock tube experiments*, J. Fluid Mech. **712** (2012), 354–383.

[53] B. J. Motl, *Experimental parameter study of the richtmyer-meshkov instability*, Ph.D. thesis, University of Wisconsin-Madison, 2008.

[54] B. J. Motl, J. G. Oakley, D. Ranjan, C. Weber, M. Anderson, and R. Bonazza, *Experimental validation of a richtmyer–meshkov scaling law over large density ratio and shock strength ranges*, Physics of Fluids **21** (2009), 126102.

[55] N. J. Mueschke, M. J. Andrews, and O. Schilling, *Experimental characterization of initial conditions and spatio-temporal evolution of a small-Atwood-number Rayleigh—Taylor mixing layer*, J. Fluid Mech. **567** (2006), 27.

[56] T. Mullin, *Turbulent times for fluids*, New Scientist **124** (1989).

[57] G. C. Orlicz, S. Balasubramanian, and K. P. Prestridge, *Incident shock mach number effects on richtmyer-meshkov mixing in a heavy gas layer*, Physics of Fluids **25** (2013), 114101.

[58] B. Petersen and J. Ghandhi, *High-resolution turbulent scalar field measurements in an optically accessible internal combustion engine*, Exp. Fluids **51** (2011), 1695–1708.

[59] S. Pope, *Turbulent flows*, Cambridge University Press, Cambridge, 2000.

[60] J. K. Prasad, A. Rasheed, S. Kumar, and B. Sturtevant, *The late-time development of the Richtmyer–Meshkov instability*, Phys. Fluids **12** (2000), no. 8, 2108–2115.

[61] K. P. Prestridge, P. M. Rightley, P. Vorobieff, R. F. Benjamin, and N. A. Kurnit, *Simultaneous density-field visualization and piv of a shock-accelerated gas curtain*, Experiments in Fluids **29** (2000), 339–346.

[62] P. Ramaprabhu and M. J. Andrews, *Experimental investigation of Rayleigh–Taylor mixing at small atwood numbers*, J. Fluid Mech. **502** (2004), 233–271.

[63] D. Ranjan, *Experimental investigation of the shock-induced distortion of a spherical gas inhomogeneity*, Ph.D. thesis, University of Wisconsin-Madison, 2008.

[64] L. Rayleigh, *Investigation of the character of the equilibrium of an incompressible heavy fluid of variable density*, P Lond. Math. Soc. **14** (1883), no. 1, 170–177.

[65] K. I Read, *Experimental investigation of turbulent mixing by Rayleigh–Taylor instability*, Physica D **12** (1984), no. 1-3, 45–58.

[66] D. Reese and C. Weber, *Numerical investigation of 3d effects on a 2d-dominated shocked mixing layer*, Physics of Fluids **28** (2016), no. 114102.

[67] R. C. Reid, J. M. Prausnitz, and B. E. Poling, *The properties of gases and liquids*, McGraw Hill Book Co., New York, NY, 1987.

[68] L.F. Richardson, *Weather prediction by numerical process*, University Press, 1922.

[69] R. D. Richtmyer, *Taylor instability in shock acceleration of compressible fluids*, Commun. Pure Appl. Math. **13** (1960), no. 2, 297–319.

[70] O. Schilling and M. Latini, *High-order WENO simulations of three-dimensional reshocked Richtmyer—Meshkov instability to late times: dynamics, dependence on initial conditions, and comparisons to experimental data*, Acta Math. Sci. **30** (2010), no. 2, 595–620.

[71] A.E. Siegman, MW Sasnett, and TF Johnston Jr, *Choice of clip levels for beam width measurements using knife-edge techniques*, Quantum Electronics, IEEE Journal of **27** (1991), no. 4, 1098–1104.

[72] W.T. Silfvast, *Laser fundamentals*, Cambridge University Press, 2004.

[73] G. Taylor, *The instability of liquid surfaces when accelerated in a direction perpendicular to their planes. i*, P. R. Soc. Lond. **201** (1950), no. 1065, 192–196.

[74] B. Thornber, D. Drikakis, D. L. Youngs, and R. J. R. Williams, *The influence of initial conditions on turbulent mixing due to Richtmyer–Meshkov instability*, J. Fluid Mech. **654** (2010), 99–139.

[75] M. Vetter and B. Sturtevant, *Experiments on the Richtmyer-Meshkov instability of an air/SF6 interface*, Shock Waves **4** (1995), 247–252.

[76] M. Vetter and B. Sturtevant, *Experiments on the richtmyer-meshkov instability of an air/sf6 interface*, Shock Waves **4** (1995), 247–252.

[77] P. Vorobieff, N. G. Mohamed, C. Tomkins, C. Goodenough, M. Marr-Lyon, and R. F. Benjamin, *Scaling evolution in shock-induced transition to turbulence*, Phys. Rev. E **68** (2003), no. 6, 065301.

[78] P. Vorobieff, P. M Rightley, and R. F Benjamin, *Power-law spectra of incipient gas-curtain turbulence*, Phys. Rev. Lett. **81** (1998), 2240–2243.

[79] C. Weber, *Turbulent mixing measurements in the richtmyer-meshkov instability*, Ph.D. thesis, University of Wisconsin-Madison, 2012.

[80] C. Weber, A. W. Cook, and R. Bonazza, *Growth rate of a shocked mixing layer with known initial perturbations*, J. Fluid Mech. **725** (2013), 372–401.

[81] C. Weber, N. S. Haehn, J. Oakley, D. A. Rothamer, and R. Bonazza, *Turbulent mixing measurements in the richtmyer–meshkov instability*, Physics of Fluids **24:074105** (2012).

[82] C. Weber, B. J. Motl, J. G. Oakley, and R. Bonazza, *Richtmyer-meshkov parameter study*, Fusion Science and Technology **56** (2009), no. 1, 460–464.

[83] C. R. Weber, *Turbulent mixing measurements in the Richtmyer-Meshkov instability*, Ph.D. thesis, University of Wisconsin-Madison, December 2012.

[84] C. R. Weber, A. W. Cook, and R. Bonazza, *Growth rate of a shocked mixing layer with known initial perturbations*, J. Fluid Mech. **725** (2013), 372–401.

[85] C. R. Weber, N. Haehn, J. Oakley, D. Rothamer, and R. Bonazza, *An experimental investigation of the turbulent mixing transition in the richtmyer-meshkov instability*, J. Fluid Mech. **748** (2014), 457–487.

[86] P. N. Wilson and M. J. Andrews, *Spectral measurements of Rayleigh—Taylor mixing at small atwood number*, Phys. Fluids **14** (2002), no. 3, 938.

[87] J. Yang, T. Kubota, and E. E. Zukoski, *A model for characterization of a vortex pair formed by shock passage over a light–gas inhomogeneity*, J. Fluid Mech. **258** (1994), 217–244.

[88] D. L. Youngs, *Numerical simulation of turbulent mixing by Rayleigh–Taylor instability*, Physica D **12** (1984), no. 1-3, 32–44.

[89] _____ , *Modelling turbulent mixing by Rayleigh–Taylor instability*, Physica D **37** (1989), 270–287.

[90] _____ , *Numerical simulation of mixing by Rayleigh–Taylor and Richtmyer-Meshkov instabilities*, Laser Part. Beams **12** (1994), no. 4, 725–750.

[91] Y. Zhou, *A scaling analysis of turbulent flows driven by Rayleigh—Taylor and Richtmyer—Meshkov instabilities*, Phys. Fluids **13** (2001), no. 2, 538.